Rock slope temperature evolution and micrometer-scale deformation at a retreating glacier margin

Marc Hugentobler, Jordan Aaron, Simon Loew

Department of Earth Sciences, Engineering Geology, ETH Zurich, 8092 Zurich, Switzerland.

Corresponding author: Marc Hugentobler (marc.hugentobler@erdw.ethz.ch)

Key points

- We monitor and model the subsurface temperature evolution and deformation in a rock slope during deglaciation.
- We observe a conduction dominated transient subsurface temperature regime adjusting to a new surface temperature following ice retreat.
- We document reversible deformation and irreversible rock mass damage and identify important drivers causing these deformations.

13 Abstract

14 In deglaciating environments, rock mass weakening and potential formation of rock slope instabilities is
15 driven by long-term and seasonal changes in thermal- and hydraulic boundary conditions, combined with
16 unloading due to ice melting. However, in-situ observations are rare. In this study, we present new monitor-
17 ing data from three highly instrumented boreholes, and numerical simulations to investigate rock slope tem-
18 perature evolution and micrometer-scale deformation during deglaciation. Our results show that the subsur-
19 face temperatures are adjusting to a new, warmer surface temperature following ice retreat. Heat conduction
20 is identified as the dominant heat transfer process at sites with intact rock. Observed nonconductive pro-
21 cesses are related to groundwater exchange with cold subglacial water, snowmelt infiltration, or creek water
22 infiltration. Our strain data shows that annual surface temperature cycles cause thermoelastic deformation
23 that dominate the strain signals in the shallow thermally active layer at our stable rock slope locations. At
24 deeper sensors, reversible strain signals correlating with pore pressure fluctuations dominate. Irreversible
25 deformation, which we relate with progressive rock mass damage, occurs as short-term (hours to weeks)
26 strain events and as slower, continuous strain trends. The majority of the short-term irreversible strain events
27 coincides with precipitation events or pore pressure changes. Longer-term trends in the strain time series
28 and a minority of short-term strain events cannot directly be related to any of the investigated drivers, but
29 changes of glacial loading and fatigue processes are considered as potential causes.

30 Keywords

31 Subsurface temperature evolution; progressive rock mass damage; paraglacial rock slope evolution, bore-
32 hole monitoring; rock slope deformation

1. Introduction

Retreating and advancing valley glaciers in alpine regions can induce both reversible and irreversible deformations in adjacent valley flanks. Several mechanisms can cause these deformations, however, glacial influence on the thermal and hydraulic boundary conditions of adjacent slopes has been identified as a major driver. In particular, as glaciers retreat, the stable thermal boundary conditions below glaciers are perturbed, which results in a “thermal shock” and long term cyclic thermal loading, that can induce long term rock mass damage (Grämiger et al., 2018; Grämiger et al., 2020). The present work is focused on field investigations of the transient thermal regime induced by glacier retreat in adjacent valley slopes, and the related subsurface deformations. This data set is key to the understanding of heat transfer mechanisms in the subsurface, the timescales over which valley flanks adjust to the new thermal boundary conditions following deglaciation, as well as the magnitudes of thermo-mechanical stresses, which can lead to long term rock mass damage. Investigating these phenomena requires high resolution measurements of subsurface temperatures and deformation, which have never been recorded in alpine regions that feature temperate valley glaciers. Additionally, thermo-mechanical deformation signals can be overprinted e.g. by hydromechanical deformation (cf. Grämiger et al., 2020), and disentangling the two requires an understanding of slope hydrology, as well as measurements of pore pressure and precipitation events.

Previous studies have used borehole temperature recordings to analyze the subsurface temperature regime and reconstruct past climate conditions (Bodri and Čermák, 1995; Bodri and Čermák, 1999; Pollack, 1993; Pollack et al., 1998; Pollack and Huang, 2000), as well as study permafrost processes (e.g., Gruber et al., 2004; Haberkorn et al., 2015; Schneider et al., 2012) and drivers of active rock slope instabilities (e.g., Gischig et al., 2011a; b; Moore et al., 2011). However, to the authors knowledge, subsurface temperature investigations in alpine environments undergoing glacial retreat below permafrost elevations have not been monitored in the past.

When considering the thermal regime of a rock slope, the glacier – rock slope interaction is controlled by both thermal and hydraulic conditions at the ice-rock interface. Bedrock in contact with temperate ice stays at the pressure melting point of the ice, which is around 0° C (Wegmann et al., 1998). When ice retreats,

the previously covered bedrock surface is newly exposed to ambient temperature variations and solar radiation. These warmer temperatures then propagate to depth through a combination of conduction and advection.

A conduction dominated subsurface temperature regime, which is expected in intact crystalline bedrock, is controlled by: 1) the surface temperature, which is subject to variability at daily to millennial timescales, 2) an outward flow of heat from the earth's interior, which can be considered constant at the relevant timescales, 3) the thermal diffusivity of the medium, 4) latent heat effects from melting ice or freezing water in pores/cracks, and 5) the topography (Guéguen and Palciauskas, 1994; Pollack et al., 1998). In the case of homogenous subsurface thermal properties and flat topography, a steady-state temperature profile shows a constant rate of temperature increase with depth (dependent on the thermal conductivity and the heat flow from below). Surface temperature fluctuations then propagate as thermal waves at a pace governed by the thermal diffusivity, with amplitudes diminishing exponentially with depth (Pollack and Huang, 2000).

In reality, rock masses contain discontinuities that allow nonconductive heat transfer processes (e.g. advection of air or water) and heterogeneities (e.g. in the lateral thermal conductivity) that potentially disturb the idealized heat conduction dominated subsurface temperature regime (Moore et al., 2011; Rybach and Pfister, 1994; Wegmann and Gudmundsson, 1999). Of particular importance to the present work are advective heat transfer processes driven by seasonal changes in rock slope hydrology in a glaciated valley, which influence the thermal regime. Transient pore pressures in such rock slopes are controlled by direct recharge to the fractured bedrock slope from snow melt in late spring and rainstorms in summer and fall, as well as by the englacial water pressure variations. Temperate glaciers carry large amounts of liquid water, and a thin water film with pressures dependent on the glacial hydrological system is assumed to be present at greater depth at the glacier – rock interface (Lappegard et al., 2006).

Different types of temperature-coupled processes such as frost weathering, freeze-thaw cycles, and permafrost degradation contribute to progressive rock mass weakening in alpine regions (Deprez et al., 2020; Draebing and Krautblatter, 2019; Draebing et al., 2017; Hales and Roering, 2007). Additionally, thermomechanical stresses themselves can drive deformation and progressive rock mass damage in an unstable

rock slope (Gischig et al., 2011a; b). In the context of post- and late-glacial ice retreat, numerical investigations suggest that purely thermo-mechanical effects induced by long-term temperature variations related to glacial cycles and seasonal temperature variations induce significant thermo-mechanical stresses to the valley flanks which promote progressive rock mass damage (Baroni et al., 2014; Grämiger et al., 2018). These studies have shown that, during a glacial cycle, thermo-mechanically driven deformation and rock mass damage can be substantially higher than purely mechanical loading and unloading effects from glacier retreat or advance, and that the degree of fracturing (and the criticality of the fracture system in terms of its Mohr-Coulomb strength) is a an important factor controlling the amount of induced thermo-mechanical damage (Grämiger et al., 2018).

Rock mass damage can also result from subcritical cyclic stress perturbations and stress corrosion (Cerfontaine and Collin, 2018; Eppes and Keanini, 2017). This has been observed in laboratory experiments and is described by several authors (e.g., Attewell and Farmer, 1973; Brown and Hudson, 1973; Cerfontaine and Collin, 2018). Thus, low stresses can also increase the criticality of a fracture to a level exceeding the fracture toughness, which enables the fracture to fail at an apparently random, low magnitude stress perturbation, complicating correlations with environmental drivers (Eppes and Keanini, 2017).

In this study we use novel borehole monitoring data and numerical simulations to investigate the transient subsurface temperature regime and related micrometer-scale deformation in a rock slope adjacent to a temperate valley glacier undergoing rapid downwasting. We first analyze the borehole temperature and strain data and perform a statistical analysis of the strain data to highlight correlations between potential drivers and deformation events. We then use the borehole temperature data to estimate the depth-dependent apparent thermal diffusivity at our borehole locations, which is used to parameterize continuum 2D finite element models for heat conduction in the subsurface. Comparing these modeling results with temperature monitoring data provides insights into the transient subsurface temperature regime that follows glacier retreat, as well as the dominant mechanisms governing heat transfer at our study site (conduction vs. advection). Finally, we expand our finite element models to compute the expected thermoelastic deformation resulting from annual temperature cycles. These analyses provide crucial information regarding the relative importance of thermo-mechanical deformation on the total strain recorded at our instrumented rock slope,

and hence its relevance for the overall observed deformation and progressive rock mass damage.

2. Site description and previous work

Our study site is located on the left (i.e. southern) valley slope adjacent to the retreating glacier tongue of the Great Aletsch Glacier (Canton Valais, Switzerland) (see Fig. 1). The bedrock consists of fractured crystalline rocks (mainly gneisses and granites with thin shist layers) of the Aare-Massif (Steck, 2011). The rock slope is dipping NNW with an average slope angle of about 30° and the morphology is characterized by glacially smoothed bedrock surfaces with ridges and furrows. Furrows often follow weak schist layers or brittle-ductile shear zones normally oriented subparallel to the alpine foliation. This foliation strikes valley subparallel with a subvertical dip angle normally dipping into the slope. The rock mass is intersected by three persistent joint sets with a normal spacing around 1 to 3 m at the ground surface (for joint set orientations refer to Fig. 4 in Hugentobler et al. (2020)).

A thin and patchy moraine layer, surrounding several rock outcrops, covers the lower study area. Due to the recent glacial retreat, no noteworthy vegetation is present in the study area. The Moosfluh instability, a well-documented deep seated gravitational slope deformation (DSGSD) with superimposed shallower rockslides, is situated in the southwest of the study area x.

The glacial history of the Great Aletsch Glacier, the largest ice mass in the European Alps, is summarized in Holzhauser et al. (2005) and glacial extents in the vicinity of the study area have been investigated in detail by Grämiger et al. (2017). Additionally, glacial retreat from the last local maxima in 1860, the Little Ice Age (LIA), is well documented by GLAMOS (1881-2019). Since the LIA, the glacier tongue lost more than 3000 m of length and over 300 m in ice thickness at the location of our study site. This leads to a mean ice height loss of about 2 m per year since LIA. However, annually acquired, high-resolution digital elevation models of the Great Aletsch Glacier area from the years 2012 until 2019 (source: Swiss Federal Office of Topography) show that the current melting rates are higher, with about 5 - 10 m ice height loss per year.

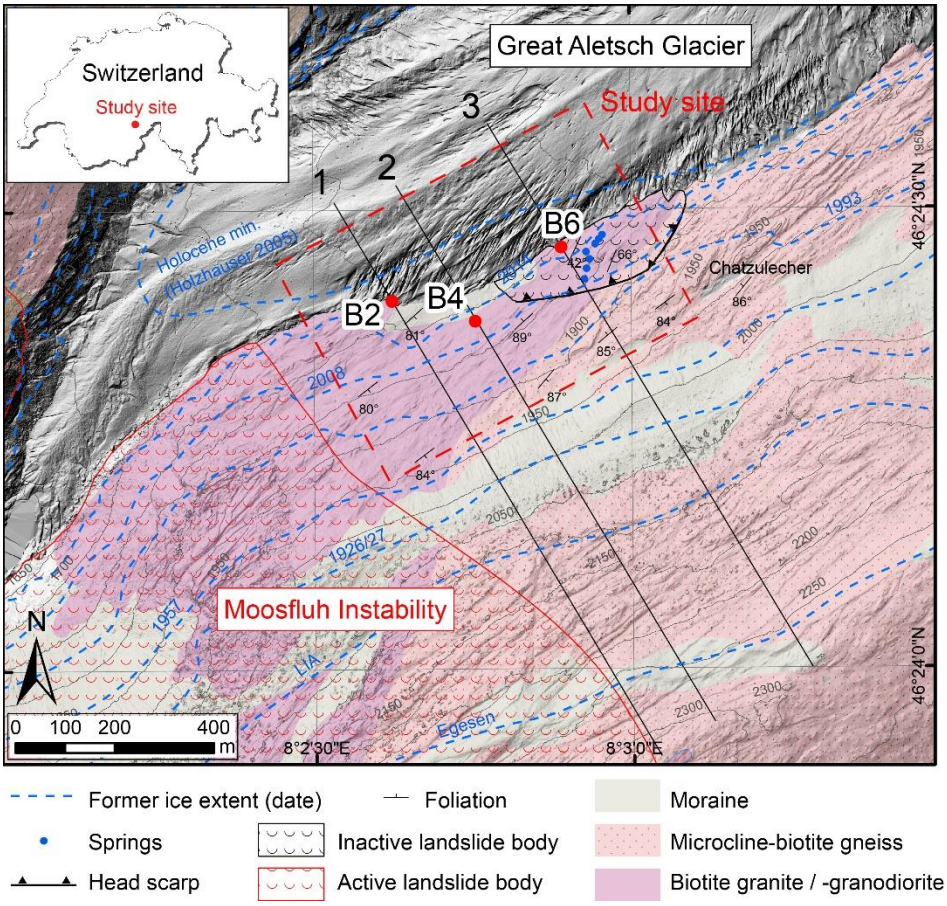

Fig. 1. Overview map of the study area at the terminus of the Great Aletsch Glacier at the Autumn 2017 ice extent with the research borehole locations B2, B4, and B6 (modified after Hugentobler et al., 2020). The former glacial extents of years 1927 to 2014 were digitized from historical aerial photos by Glueer et al. (2020) and the Little Ice Age (LIA) and Egesen maximum extents are well constraint by lateral moraines in the map area. We extended the geological map from Steck (2011) in the area that had been glacier covered during their mapping campaign. The numbered solid black lines are the extents of the 2D profiles used for the numerical study.

A subsurface monitoring system has been installed to investigate and quantify the effects of thermo-hydro-mechanical rock slope processes that occur along with downwasting and retreat of glacial ice (Hugentobler et al., 2020). The monitoring system is installed in three vertical, 44 to 50 m deep instrumented research boreholes of 10 cm diameter (B2, B4, and B6, see Fig. 1). The three borehole locations were selected to have varying lateral distance to the glacier margin, so that they monitor the rock slope conditions at different timings relative to deglaciation (**Fehler! Verweisquelle konnte nicht gefunden werden.**), and in slope sectors of different degree of stability and damage. Before the recent deglaciation, the borehole locations

were ice covered for approximately 2000 to 3000 years (Holzhauser et al., 2005).

The boreholes are fully grouted, and contain high resolution vertical and horizontal strain sensors, a temperature sensor chain, and a pore pressure sensor installed in a 1 – 2 m long sand filter at the borehole end. The setup and performance and early data of the monitoring system is described in detail in Hugentobler et al. (2020). Air temperature is measured at our study site with a 30 min interval and total precipitation data used in this study is provided by MeteoSchweiz and recorded at the weather station "Bruchji" (canton Valais) located about 6 km away from our study site.

The rock mass and the hydrogeological properties at our study site have been characterized with surface structural mapping, rock mass classifications (at outcrops surrounding the borehole sites and from borehole optical televiewer images), borehole geophysical and hydro-geophysical investigations, as well as pumping and injection tests in the boreholes. These analyses have identified differences between the three research borehole locations (Hugentobler et al., 2020). The main findings for the individual boreholes related to rock mass quality are summarized below. As the boreholes were drilled in 2017, references to the glacier position refer to those present during that year.

- Borehole B2 was drilled directly at the ice margin at the end of a relatively flat plateau and only about 200 m away from the active Moosfluh slope instability. Optical televiewer images of the borehole wall reveal a high fracture density with open joints often filled with fines in the uppermost 20 m (Fig. 2). Below this depth, fractures occur less frequently and with lower aperture. The rock mass at outcrops surrounding B2 was classified with a Geological Strength Index (GSI) between 55-65. According to the optical televiewer image, these values can be confirmed for the upper part of the borehole, but slightly increase with depth due to the decreasing fracture density (Fig. 2). From a borehole water injection test, the transmissivity in the lower part of the borehole (around 15 to 50 m depth) was estimated around 10^{-6} m^2/s and in the uppermost, fractured part around 10^{-3} m^2/s.
- Borehole B4 is located about 50 m away from the glacier margin at a relatively evenly dipping slope. Borehole optical televiewer logs show that the rock mass is less fractured compared to B2 (Fig. 2), with mainly closed or low aperture structures. A surficial layer of about 5 m with a dense fracturing is present at this location (Fig. 2). GSI values at outcrops around B4 reveal a high-quality rock mass

with values between 75 and 85. Similar to B2, the rock mass quality appears to increase with depth with the observed decrease in fracture density. A pumping test in the borehole revealed a transmissivity of about 10^{-6} m^2/s between 9 and 44 m depth and higher assumed values in the uppermost section. Fluid electric conductivity logs show a major transmissive structure at the depth of 29.4 m and minor transmissive structures at 19.5 m, 25 m, and 39.8 m.

- Borehole B6 was drilled at a cliff position with about 5 m lateral distance to the glacier margin. The area around the borehole is characterized by a disturbed rock mass bounded by a prominent head scarp above (see Fig. 1). Surface structural mapping indicates that this area is likely an inactive toppling rock slope instability, hosting important groundwater springs. We estimated GSI-values at outcrops around B6 to range between 50 and 60. Because of unstable borehole conditions, a perforated PVC casing was installed in the borehole (cf. Hugentobler et al., 2020). Therefore, only fluid electric conductivity logging and a pumping test could be conducted. These tests resulted in an estimated borehole transmissivity of around 10^{-5} m^2/s with higher assumed values in the top layer and major transmissive structures at a depth of 35.5 m and 43 m. A surface creek that originates from springs located a few tens of meters above the borehole location passes a depression next to the borehole and was observed to infiltrate through fractures into the borehole during drilling works. The lower GSI-values, the higher transmissivity, and the borehole stability issues encountered while drilling reveal the lower rock mass quality at this borehole location compared to the other two.

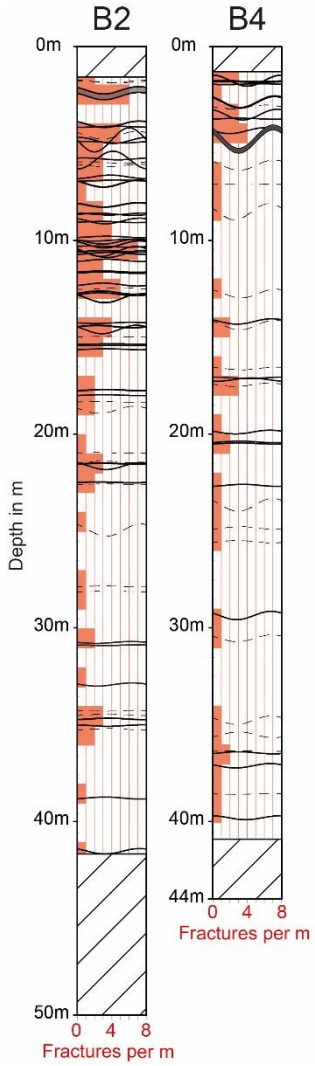

Fig. 2. Illustration of structures mapped on the optical televiewer image in borehole B2 and B4 (modified after Hugentobler et al., 2020). An optical televiewer image of B6 does not exist because no such survey could be conducted in this borehole. Solid black lines in the log indicate major discontinuities such as open joints, filled joints, sheared and fractured zones. Dashed lines indicate minor discontinuities (e.g., closed or healed joints). Red bars show the fracture count per m along the borehole.

3. Methods

3.1. Analysis of monitoring data

In this paper, we present a detailed analysis of data from the subsurface temperature sensor chains, as well as from the high resolution vertical FBG strain sensors. Subsurface temperatures have been recorded since

October 2017 with an hourly measurement interval, and a downhole sensor spacing of 1 m. Some data gaps of a few weeks in total exist in the time series that are related to battery issues. One longer data gap of four months (April to July 2018) in the B2 time series is related to a temporary glacier re-advance that overran the borehole location and disrupted the loggers from the sensor chains.

We use the subsurface temperature data to empirically estimate the in-situ apparent thermal diffusivity D within the annual thermally active layer. D is defined as $D = \lambda/(\rho C_P)$, where λ is the thermal conductivity, ρ the density of the rock mass, and C_P the specific heat capacity of the rock. This was done by analytically solving the 1D heat conduction equation for measured periodic surface temperature forcing, and fitting our subsurface temperature data (cf. Koo and Song, 2008; Rajeev and Kodikara, 2016; Schneider et al., 2012). The analytical solution can then be inverted to estimate apparent thermal diffusivity based on measurements of either the amplitude decay or phase delay of the propagation of a thermal signal with depth. We apply both of these inversion procedures and use the results to interpret which borehole locations are conduction dominated, as well as to parametrize our 2-D continuum heat transfer models.

The FBG sensors are installed as a serial connection of ten individual sensors with base lengths of 4 to 5 m and cover the full length of each borehole. The individual strain values were calculated by averaging over hourly dynamic measurements of approximately 30 s duration. In Hugentobler et al. (2020) we introduced the strain signals measured with the FBG-system and showed that the system is capable to reliably detect strains down to a magnitude below 1 με (or 4 µm). The individual FBG strain sensors show long term continuous changes in strain (extension and contraction), distinct short-term strain events (within hours to days), and rapid strain steps (within one measurement cycle of 1 h) (Fig. 6, Fig. A 1, A 2, and A3). We use a principal component analysis (PCA) with the aim to investigate the continuous, longer-term strain changes and an event detection procedure for the short-term and rapid strain variations (hereafter called strain events). An explanation of these different strain signals is provided in the beginning of section 4.1.3.

PCA is an exploratory statistical method that can be used to synthesize information contained in our large number of datasets (e.g., Govaert, 2009). A PCA was run for all three boreholes separately based on centered and standardized data matrices containing time series of the ten FBG-sensors. The resulting principal

components were then correlated with potential drivers, including measured surface temperature, pore pressure and precipitation, in order to understand the relationship between these potential drivers and the measured strain.

To investigate potential drivers for strain events in the data and their distribution over the year, the timing of the most significant strain events in the time series were automatically retrieved with the MATLAB function findchangepts. This function finds the most significant changes in mean and slope of a time series based on a predefined maximum number of changing points, or a change threshold. All automatically detected strain events were then manually checked. A minority of detected events were corrected because they were artifacts related to data gaps, but the majority were confirmed. The timing of these strain events was then compared to the same potential drivers as used for the PCA. We expect that the drivers of strain events may be depth dependent, so we distinguish deep and shallow strain events. This allows us to analyze the different drivers of short term and rapid strain events, which are potentially related to rock mass damage.

3.2. Numerical simulation

We performed 2D, finite-element numerical modeling in order to understand long term (on the order of 200 years) changes of the slope thermal regime caused by glacial retreat, as well as yearly changes in the thermal regime, and resulting thermo-elastic strain, driven by seasonal temperature cycles. 2D numerical simulations were conducted using the commercial finite element software COMSOL Multiphysics v 5.5. The model geometry was defined using 2D cross-sections that intersect the three borehole sites, and laterally extend from the glacier-filled valley bottom to the ridge of Moosfluh/Hohfluh (see Fig. 1). Surface topography above the current glacial ice level was defined using a high-resolution DEM from 2018 of the study area (source: Swiss Federal Office of Topography). Elevations of bedrock sections currently covered by glacial ice were interpolated using data from Rutishauser et al. (2016) in GlaThiDa_Consortium (2019).

Heat conduction is the only heat transfer process occurring in our continuum models. The transient subsurface temperature field in the model was calculated by assigning boundary conditions (BC) of a constant geothermal heat flux at the bottom, a transient surface rock temperature at the top (described in more detail below), and no-flow lateral boundaries (Fig. 3). To achieve a realistic geothermal gradient of ~23 °C km^{-1} in depth (cf. Rybach and Pfister, 1994), the geothermal heat flux at the bottom boundary of the model was set

to 60 mW m^{-2} which agrees to values used in literature (Wegmann et al., 1998).

Our models then solve the heat conduction equation defined as $\partial T/\partial t = D\nabla^2 T$ for the model domain. The thermal diffusivity D was mainly based on the empirical estimation described in the previous section, and the C_P and ρ values used in the 2D model are based on literature values, as summarized in Table 1.

We used a depth dependent thermal diffusivity in our models to partially account for the depth dependent structural heterogeneity present at our study site. Between 0 and 10 m depth we assigned the mean estimated in-situ value based on the inversion procedure detailed above. From 20 m downwards a constant literature value for intact rock thermal diffusivity was used (Table 1), and in between these two values the thermal diffusivity was linearly interpolated.

Table 1. Literature parameters used for the numerical simulations.

Thermal properties		
Specific heat capacity C_P (at constant pressure)	780 J kg^{-1} K^{-1}	Wegmann (1998)
Thermal conductivity λ (intact rock)	2.9 W m^{-1} K^{-1}	Wegmann et al. (1998)
Mechanical properties		
Density ρ	2700 kg m^{-3}	Wegmann et al. (1998)
Poisson's ratio	0.2	Grämiger et al. (2017)
Young's modulus	30 GPa	Grämiger et al. (2017)
Thermal expansion α	9.5 * 10^{-6} K^{-1}	Keusen and Amiguet (1987)

The numerical modeling was performed in four steps, with the different boundary conditions visualized in Fig. 3 and the thermal boundary conditions detailed in Table 2 :

1. The steady-state subsurface temperature field was calculated for the LIA ice extent (see Fig. 9a) using 0° C at the top boundary below ice elevation (BC1) and above the ice elevation an elevation dependent mean annual ground temperature (MAGT) function (BC2).
2. Starting from the steady-state temperature field of modeling step 1, a transient model was run to simulate the thermal effect of the lateral ice retreat from the LIA (~1860) to the 2017 ice extent. Historical aerial photos show that the lateral ice retreat along our modeled profiles correlates linearly with the documented glacier length change of the Great Aletsch Glacier (GLAMOS, 1881-2019), which has

been monitored in detail. Therefore, the rate of glacial length change was used to calculate the lateral ice extent in each time step of the model. With this method, the modeled timing of deglaciation at the borehole locations deviate by a maximum of 2 years compared to the actual year of deglaciation. A constant temperature of 0° C (BC1) was assigned to the part of the top boundary below this lateral ice extent, and an elevation dependent MAGT function (BC2) was assigned above.

3. Following the simulation of ice retreat from the LIA, seasonal temperature variations were modeled using the measured temperature recorded at the uppermost sensor of borehole B4 (BC3), superimposed on the long-term deglaciation trend since LIA. In this modeling step, the temporal resolution was increased to 1 hour in order to investigate the effects of seasonal temperature cycles on the subsurface temperature field. Similar to modeling step 1 and 2, BC1 was assigned at the top boundary below glacial ice. To achieve the best possible fit of the initial conditions with measured temperatures in borehole B4 we tweaked the model parameters for modeling step 2 (LIA retreat) by using a constant intact rock thermal diffusivity of $1.4*10^{-6}$ m^2/s instead of the 2-layer thermal diffusivity. Then modeling step 2 was run for 158 years (1860 (LIA) to 2018). Following this, we applied a spin-up period of one annual cycle using again the 2-layer thermal diffusivity and BC3 top condition (Table 2) to allow the models' initial conditions to get balanced with the boundary conditions. For the simulation of the seasonal temperature cycles we then used the 2-layer thermal diffusivity introduced above.

Table 2. Used thermal boundary conditions (BC) to model 2D heat conduction in our glacier adjacent rock slopes.

BC #	Description	Value	Notes
BC1	Temperature below ice elevation	0° C	Elevation dependent gradient adapted from Grämiger et al. (2018) with absolute temperature values fitted to surface temperature monitoring data at our borehole location
BC2	MAGT above ice elevation	MAGT(z)=12.55-0.005*z [°C]	
BC3	GT above ice elevation	$T(t,z)=8.975-0.005*z+T_{TopB4}(t)$	

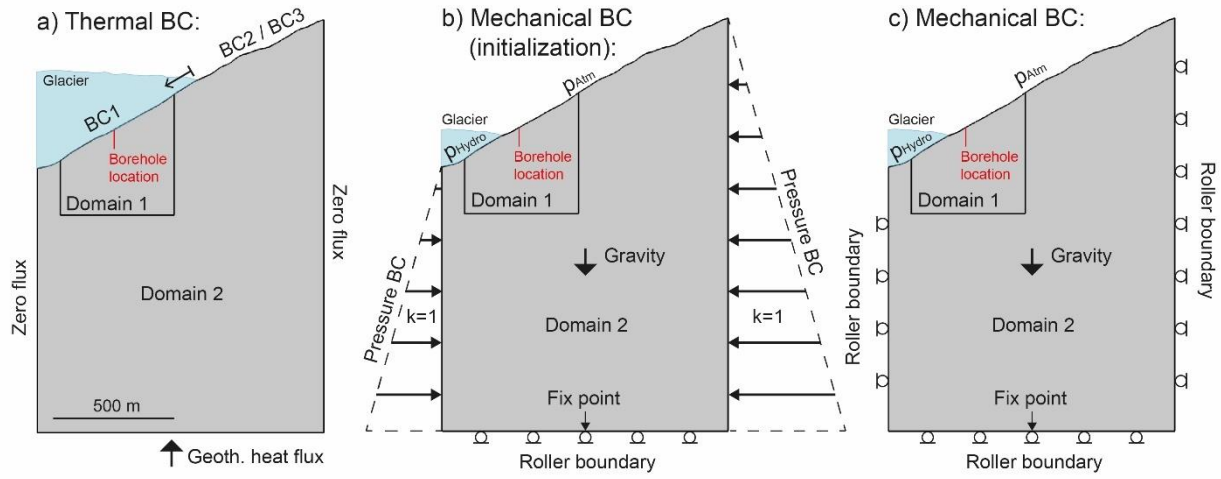

Fig. 3. Visualization of the model geometry and thermal (a) and mechanical (b and c) boundary conditions (BC) used for the numerical simulations. BC1, BC2, and BC3 are described in Table 2. Domain 1 contains a fine mesh with mesh sizes between 0.03 m and 18 m. Domain 2 contains a coarser mesh with individual mesh sizes between 0.5 m and 95 m. The mesh size is increasing with normal distance to ground surface.

4. Following the thermal modeling steps 1 to 3, we computed the expected thermoelastic strains resulting from seasonal surface temperature cycles measured at our site. We used a simplified continuum modeling approach and homogenous and isotropic elastic rock mass properties, following Grämiger et al. (2017) (see Table 1). The thermo-mechanical modeling was conducted in two steps using the same model geometry as for the thermal models. First, we initialized the stresses in the rock slope with a steady-state simulation applying mechanical forces only. Far-field stresses that are of tectonic and exhumation-induced origin were modeled in a simplified way with a horizontal to vertical stress ratio of k= 1 (Kastrup et al., 2004) at the lateral boundaries of the model (Fig. 3b). We applied a roller boundary at the bottom and a fix point constraint at the center of this boundary line to keep the model in place. In addition, we added gravity and modeled a constant glacier load at the 2017 ice extent as a hydrostatic stress boundary (cf. Grämiger et al., 2017). After initialization, we switched the lateral mechanical boundaries to roller boundaries (see Fig. 3c) and calculated the thermal modeling step 3 including a thermo-mechanical coupling through the thermal expansion coefficient α. We used the same thermal initial and boundary conditions as described in modeling step 3.

4. Results

4.1. Subsurface monitoring data

4.1.1. Temperature data

Fig. 4 shows the subsurface temperature evolution of the glacier adjacent rock slope from 2018 to 2020 at the three borehole locations. The graphs in the three first columns of the figure (a, b, c, e, f, g, i, j, k) show the annual temperature variation in the form of monthly mean temperature profiles and the graphs in the column to the right of the figure (d, h, l) show the evolution of the annual mean temperatures of the three monitored years. Since we started to monitor the temperature in fall 2017, our provided annual temperature cycles start in November and end in October of the following year (e.g. 2018 contains data from Nov. 2017 until Oct. 2018). Fig. 4 shows that the depth of the thermally active layer in B2 and B4, is around 17 m, and annual temperature cycles smoothly diffuse into the subsurface. In contrast, in borehole B6 the annual thermally active layer is around 28 m deep, and the temperature profile is highly irregular. All three boreholes show weak positive and negative temperature anomalies along the profile.

Borehole B2 is the closest of the three boreholes to the glacier margin, and showed the lowest mean surface temperature in 2018 and a clear warming trend in the two following years. This warming trend is likely related to the significant change of distance to the glacial ice at this borehole location (from 0 m in 2017 to about 40 m in 2020). The annual variability in this borehole is around of 7 to 8 °C at the uppermost sensor. B4, which is the borehole located furthest from the glacier, shows a mean surface temperature of around 4 °C with an annual variability of around 8 to 9 °C. B6 has an intermediate distance to the glacier, and shows an annual mean surface temperature of around 3 °C and a variability of around 9 °C. All three boreholes display a general warming trend, which can be observed as a shift in positive direction of the mean annual temperature profiles between 2018 and 2020 (Fig. 4d, h, l). This warming trend can be overprinted by annual temperature variations in the uppermost borehole sections (e.g. boreholes B2 and B6).

The slopes of the mean annual temperature profiles in the three boreholes reveal that the warming front has propagated to different depths in each of the three boreholes. Starting with B2, Fig. 4d shows a negative temperature gradient (i.e., cooling downwards) to a depth of about 17 m (in 2018 and 2019). Between 17

m and 25 m, the temperature during these years were anomalously low, with measured values around 0 °C in years 2018 and 2019, and showing a clear increase in 2020. Below 25 m the temperature increases with depth with a gradient of about 0.2 °C / 10 m (i.e., similar to the assumed geothermal gradient of 23°/km in the area (Rybach and Pfister, 1994)).

In B4, the temperature profile (Fig. 4h) shows a cooling downward gradient along the whole length of the borehole, although this gradient reduces with depth. This reduction indicates that the trend may switch to warming downward below the borehole depth, similar to the trend observed in B2 below 25 m.

Borehole B6 shows a general temperature decrease with depth below a depth of 10 m, however, with a more irregular shape of the temperature profile showing deviations in positive and negative directions. It is important to mention that the upper 27 m of borehole B6 were not grouted until August 2018, because significant quantities of grout were lost though transmissive structures during the initial campaign in October 2017 (cf. Hugentobler et al., 2020). The open borehole and the exothermal reaction during the second grouting campaign in August 2018 influenced the B6 temperature measurements in the upper 27 m in 2018. Nevertheless, 2019 and 2020 measurements of this borehole are considered to reflect the undisturbed in-situ subsurface temperatures at this location.

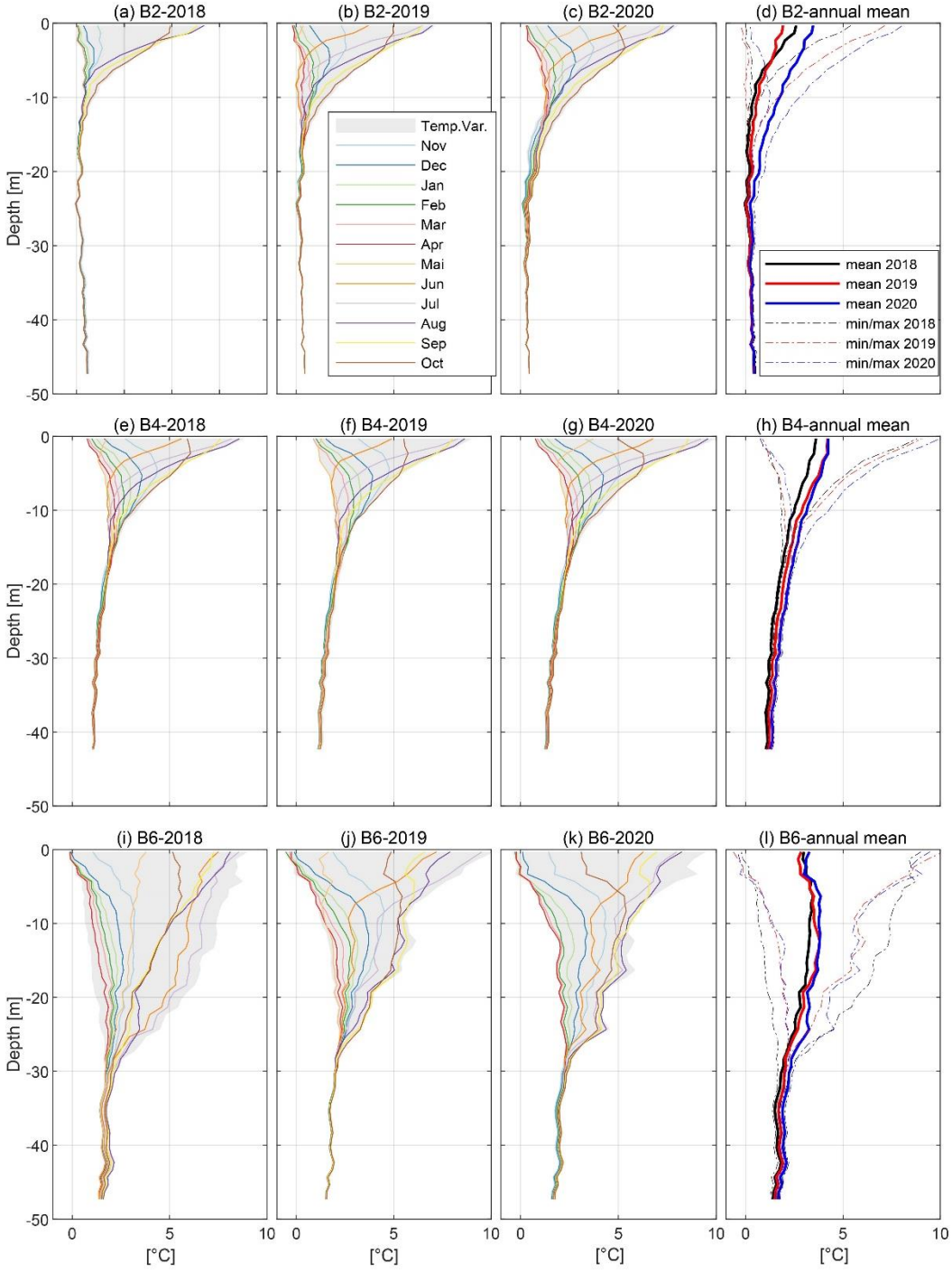

357

358 Fig. 4. Borehole temperature monitoring data of years 2018, 2019, and 2020 provided as monthly mean temperature
359 profiles (colored lines) for the three research boreholes (B2: plots a, b, c; B4: plots e, f, g; B6: plots i, j, k). The annual
360 temperature variability is illustrated in gray in the background. An annual temperature cycle presented in these plots
361 contains monthly mean temperatures starting from November of the previous year and end in October of the year

provided in the respective title. Plots d, h, l show the annual mean temperatures of years 2018, 2019, and 2020, as well as the minimum and maximum temperatures measured at each depth, for all the three boreholes.

4.1.2. Thermal diffusivity

Fig. 5 shows the results of the thermal diffusivity inversion based on periodic annual temperature cycles measured during 2019, which include separate estimates based on amplitude decay (Fig. 5a), phase delay (Fig. 5b), and their theoretical relationship (Fig. 5c). These results show a regular amplitude damping and phase delay with depth in boreholes B2 and B4, while B6 shows strong deviations from the one-dimensional heat diffusion model. Fig. 5c also shows that the annual temperature signal measured in B2 and B4 plots closely on the theoretical line, suggesting that conductive heat transfer dominates in these two boreholes. Temperature data measured in borehole B6 does not follow this theoretical relationship, hence, nonconductive processes clearly dominate the subsurface thermal regime in the upper 20 m of this borehole.

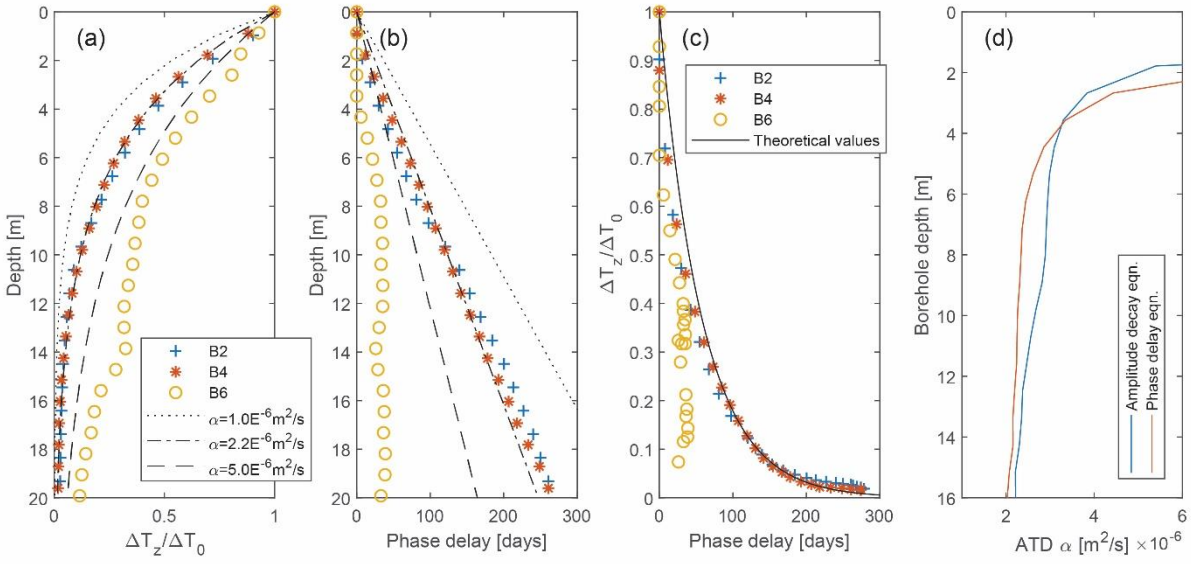

Fig. 5. The plots a, b, and c show the annual variation of the subsurface temperature driven by periodic surface temperature variations. The black, dashed, dotted, and solid lines correspond to theoretical values calculated from an analytical solution of the one-dimensional heat conduction equation for a number of apparent thermal diffusivity values α. The colored markers in the plots indicate the annual temperature variations monitored in our research boreholes in year 2019. (a) Amplitude decay of a periodic annual thermal signal vs. depth to ground surface. (b) Phase delay of a periodic annual thermal signal vs. depth to ground surface. (c) Relationship between phase delay and amplitude decay. (d)

Estimated apparent thermal diffusivity over depth for borehole B4 data using the 1-D heat conduction equation. The blue line corresponds to the estimation using the amplitude decay in the measured temperature data. The red line corresponds to the estimation using the phase delay in the measured temperature data. The apparent thermal diffusivity values represent the estimates from the depth interval between the uppermost sensor and the given depth in the y-axis.

The best fit values for the mean apparent thermal diffusivity are $2.1*10^{-6}$ m^2/s for B2 and $2.2*10^{-6}$ m^2/s for B4, respectively. Around B4, the slope shows a relatively constant dip angle, so the 1-D approach is likely more reliable at this location compared to B2, where 2-D effects are assumed to play a more important role. Therefore, the apparent thermal diffusivity estimate of B4 was used for further investigations.

Fig. 5d shows the inverted depth dependent apparent thermal diffusivity for B4, based on both the amplitude decay and phase delay. The estimates from both methods show a similar trend, with decreasing apparent thermal diffusivity values with depth. The highest values occur in the uppermost 4 m and below a more gentle decrease with depth is observed. The estimated magnitudes of thermal diffusivity are higher than literature values for conductive heat transfer in intact gneissic rocks would suggest (~ $1.4 *10^{-6}$ m^2/s) (Wegmann et al., 1998; Wegmann, 1998). We expect the estimated apparent thermal diffusivity values within the thermally active layer to approach a more constant value close to the intact rock thermal diffusivity at greater depth. Hence, the higher estimated value is assumed to be an 'apparent' value that also comprises effects related to the increased fracture density and water / air content in the surficial layer that allow minor nonconductive processes to occur. Such minor nonconductive effects should not be confused with stronger advective heat transfer processes, which are likely important in B6 and can result in significant disturbances of the diffusive profile (e.g., Ge, 1998).

4.1.3. Strain data

We measure both short- and long- term strain signals in the FBG monitoring data, which can be either reversible or irreversible. Two characteristic examples are provided in Fig. 6, and the complete FBG strain time series of all sensors in the three boreholes are provided in the Appendix (Fig. A 1, A 2, and A 3). In the present work, we interpret irreversible deformation as a proxy for rock mass damage (cf. Hugentobler et al., 2020 and references therein). Shallow sensors show annual cyclic strain components (e.g., Fig. 6a) and many sensors show a general, long term shortening trend in the 2.5 years' time series (Fig. 6a and b). Short-

term and rapid strain events, indicated with arrows in Fig. 6, are superimposed on these longer-term signals. Some of these strain events (typically showing magnitudes of up to around 20 με) are irreversible (e.g. green arrow in Fig. 6a), whereas others are reversible at timescales from hours to several weeks (e.g. blue arrows in Fig. 6b). Reversible events often also contain a minor irreversible strain portion. The analyzed timeseries also contain a few larger irreversible strain events with magnitudes between 50 to a few 100 με. These large events occur most frequently in borehole B2 (Fig. A 1, Appendix), and could either be significant damage events, or an artefact of the FBG signal processing. Most of these steps could either be verified by simultaneous deformation detected with the independent in-place inclinometer system in the borehole (cf. Hugentobler et al., 2020), occurred at several FBG sensors simultaneously, or coincided with potential triggers. Hence, they are interpreted as significant damage events. Only one particular large step in sensor FBG-4 of borehole B2 (small form letter a in Fig. A 1) is likely a signal processing artefact and was removed in the analyses that follow.

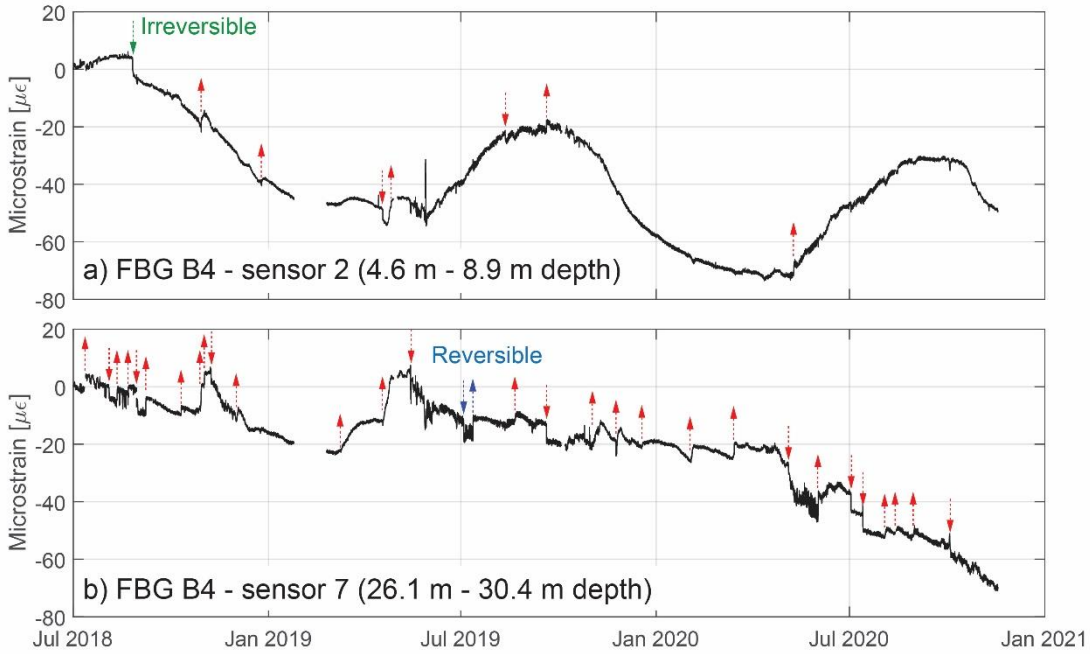

Fig. 6. Time series of two FBG strain signals measured at different sensors in borehole B4. The complete strain data of all sensors is provided in the Appendix (Fig. A 1, A 2, and A 3). Arrows indicate the timing and direction of short-term

and rapid strain events referred to in the text. An example for a mainly irreversible strain event is shown in panel a (green arrow). An example for a mainly reversible strain event is indicated in panel b (blue arrows).

The results of the PCA are shown in Fig. 7, and, similar to the example signals provided on Fig. 6, display both linear trends and cyclic signals that are contained in the strain time series. In all three boreholes the first principal component (PC1) shows a general shortening trend with no cyclic behavior that explains between 50% to 70% of the total variance in the strain variables. The second or third principal components in B4 and B6 display annual cyclicity, and are moderately correlated with measured ground temperatures (the correlation values range from 0.70 (PC3) for B4 to 0.65 (PC2) for B6). These components explain 13% (B4) and 20% (B6) of the total variance of the measured strain. In B2 the third component (PC3) shows the relatively low maximum linear correlation coefficient of 0.3 with ground temperature, which explains only around 10% of the total variance in the strain signals. No clear correlation with other potential drivers for deformation (e.g. pore pressure variations or precipitation events) can be detected. In B2 no correlation with the pressure head can be investigated because no functioning pore pressure sensor is installed (cf. Hugentobler et al., 2020).

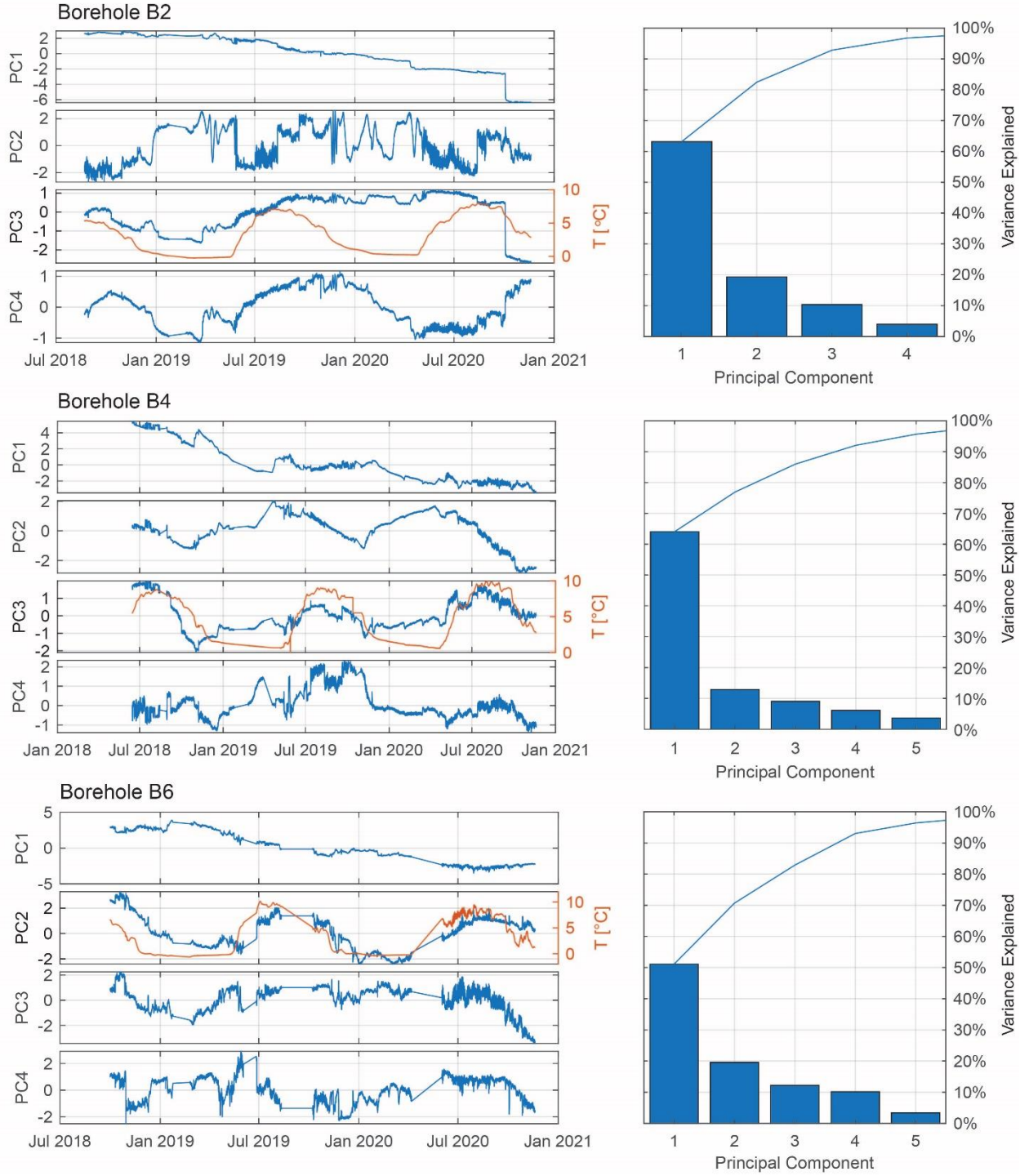

Fig. 7. Plots of scores containing the principal components 1 to 4 for the strain measured in the three boreholes B2, B4, and B6 (left column). For each borehole, a histogram (including the cumulative sum; blue line) is provided that shows how much of the total signal variance can be explained by the individual principal components (right column).

Fig. 8 presents a comparison of detected strain events measured with the FBG-sensors to potential drivers for deformation, which include surface temperature, pressure head, and precipitation. The data shows that, depending on the borehole, between 60 and 75 % of the strain events coincide with precipitation events (Fig. 8b, f, and j). Only about half of these precipitation events caused a clear pressure head increase (Fig. 8e and i). On the other hand, 5 to 10 % of the strain events temporally correlate with pressure head increases not related to direct rainfall infiltration but to snowmelt infiltration. Very few strain events (< 2 %) coincide with extreme surface temperatures (Fig. 8a, d, and h). These results emphasize the importance of hydro-mechanical and potentially moisture-related processes for deformation, however the interactions are likely complex, as rainfall would also modify the mechanical and hydraulic glacial boundary conditions. Analyzing these complex interactions is beyond the scope of the present paper, but will be explored in a future contribution.

Between 20 to 30 % of the strain events do not coincide with any of the three potential triggers. To investigate if these events could be related to earthquakes, which are also frequently discussed as destabilizing factors during deglaciation (e.g., McColl and Draebing, 2019), we compared the timing of the strain events with measured earthquakes in the time period (data provided by the Swiss Seismological Service, SED). Earthquakes that occurred at epicentral distances less than 50 km from the study site and having magnitudes greater than M1 and an earthquake depth of less than 15 km were used for the comparison. However, we did not find any correlation between the around 70 recorded earthquakes during the monitoring period (maximum magnitude M3) and the measured strain events in our boreholes. A characterization of all earthquake events used for the comparison (i.e., magnitude, epicentral distance to study site, and earthquake depth) can be found in the Appendix (Fig. B 1).

The cumulative numbers of detected strain events (Fig. 8c, g, and k) allow us to better visualize the variation of the number of events occurring over the year. Data in these plots is provided as mean number of strain events per sensor interval for shallow sensors (within the annual thermally active layer, i.e. the uppermost ~ 18 m) and for deep sensors (~18 m down to the borehole end). Fig. 8 shows that fewer strain events occur during wintertime compared to the spring and summer season and that these strain events occur more

466 frequently in deeper sensors. This difference between shallow and deeper sensors is more strongly pro-
467 nounced in B4 and B6 compared to B2. In B2, some large magnitude strain events are measured in the
468 shallow layer (see Fig. A 1, Appendix).

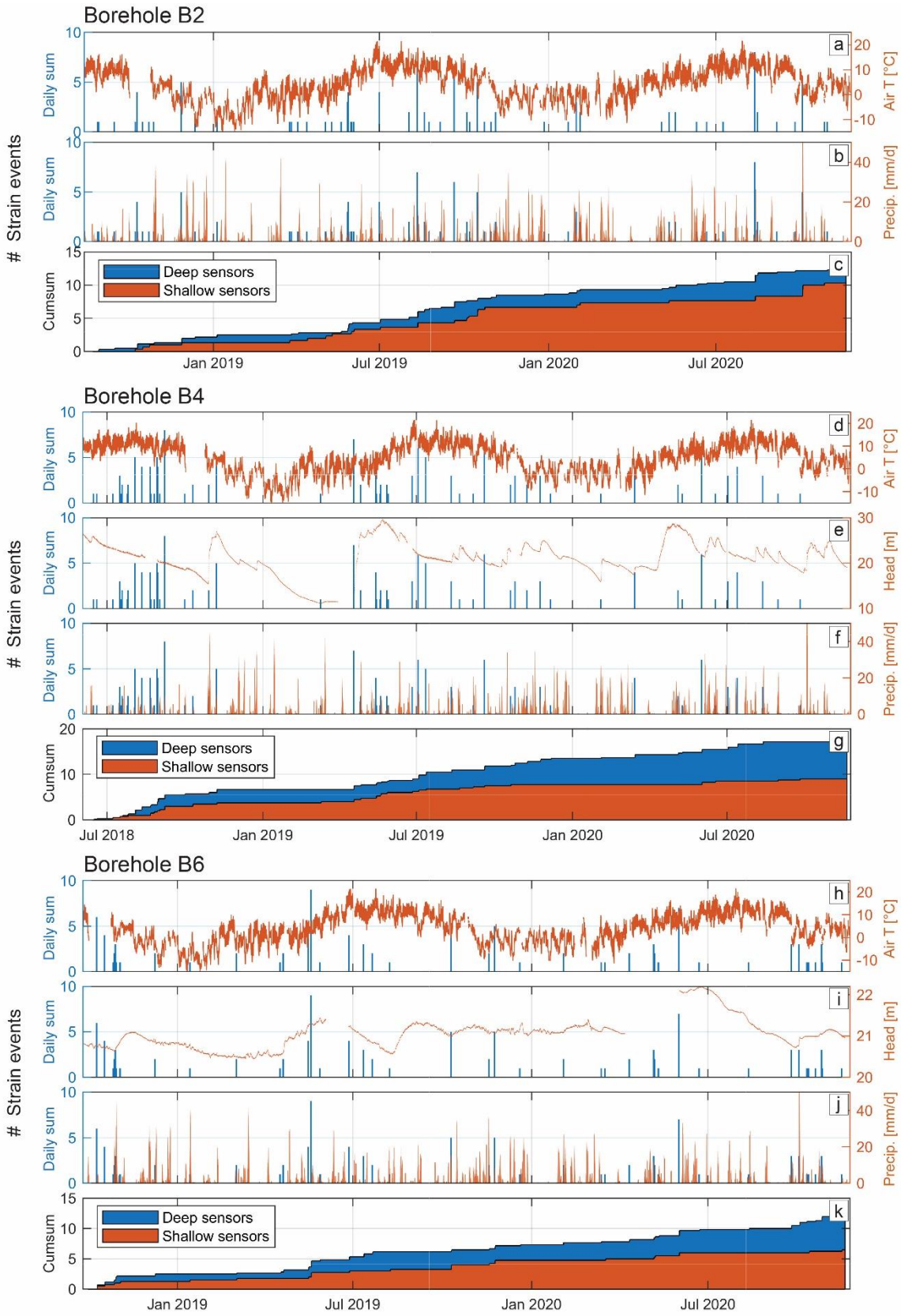
Strain events
Borehole B2
Daily sum
Air T [°C]
Precip. [mm/d]
Cumsum
Deep sensors
Shallow sensors
Jan 2019
Jul 2019
Jan 2020
Jul 2020
Borehole B4
Head [m]
Jul 2018
Borehole B6

469

Fig. 8. Number of detected strain events during the monitoring period in the three boreholes compared to potential drivers for deformation. Panels a, d, h: Daily sum of events vs. air temperature at the study site. Panels e, i: Daily sum of events vs. pressure head measured at the borehole end. Panels b, f, j: Daily sum of events vs. cumulative total precipitation per 24 h measured around 5 km away from the borehole location at the weather station "Bruchji", canton VS (provided by MeteoSchweiz). Panels c, g, k: Mean cumulative sum of events per sensor provided for "shallow sensors" (i.e., down to 18 m depth) and "deep sensors" (i.e., from 18 m down to the borehole end).

4.2. Modelling temperature evolution and deformation during deglaciation

4.2.1. Drivers of temperature evolution since LIA

Fig. 9 shows simulated subsurface temperatures during LIA deglaciation compared to our measured mean subsurface temperatures at the borehole locations. Fig. 9a shows the temperature field of the steady-state solution at the LIA ice extent, which, as mentioned previously, is used as an initial condition for the following transient ice retreat simulation. The modeled temperature field in 2019 is shown in Fig. 9b. Fig. 9c illustrates the change of the subsurface temperature profile at the specific indicated mid-slope location during glacial retreat.

As can be seen on Fig. 9c, the subsurface temperature profile before deglaciation shows 0° C at the ground surface (BC1 below ice) with a nearly linear temperature increase with depth. As soon as the ice retreats below position c, a new mean annual ground temperature is applied to the model (BC2 in Table 2) which results in warmer surface temperatures that penetrate downward with time. The adaption of the subsurface temperature to a new, warmer MAGT causes a transient inverse gradient in the upper subsurface temperature profile (i.e. cooling downwards), which transitions to a positive geothermal gradient at depth. Hence, an inverse thermal profile can be an indication for a transient subsurface temperature adapting to a new, warmer surface temperature (e.g., Pollack et al., 1998). The dashed line in Fig. 9c illustrates a newly approached steady-state temperature profile assuming the new MAGT of around 2.6° C to be constant over a very long time at the elevation of the profile. The time required to reach this new steady-state temperature profile is dependent on the thermal diffusivity of the medium.

In order to allow a meaningful comparison of modeled temperatures with temperatures measured in the boreholes, the uncertainty related to the timing of deglaciation resulting from the lateral ice retreat function

(max. 2 years, cf. section 3.2) was corrected to get the true year of deglaciation in the models. Consistent with the results shown on Fig. 9c, all the measured temperature profiles show an inverse temperature gradient at least in the upper part of the borehole, which reflects the preserved cold temperature from the glacial occupation at depth and a more recent warming trend.

Fig. 9d shows that the measured temperature profile of B2 is not exactly reproduced with our conduction model and the applied boundary conditions. However, the modelled shape of the profile and depth of the warming front is similar to that measured at this borehole location (Fig. 9d). The measured temperature profile is shifted by about 0.4° C to colder temperatures compared to the modeled values and has temperatures of around 0° C at a depth of 20 to 25 m.

Annual mean temperatures measured in borehole B4 can be well reproduced by the conduction model (see Fig. 9e). Nevertheless, the model shows a slightly slower warming at a depth below the annual thermally active layer and the borehole end. The measured temperature profiles within the thermally active layer (i.e. the uppermost ~ 20 m) deviate from the model because temperatures at these depths are subject to annual temperature variability that can differ from the used MAGT in the model.

Conversely, the measured temperature profile of B6 cannot be reproduced with our thermal conduction models. The measured temperature profile in this borehole shows a very different shape and quicker warming of the subsurface compared to the simulated ground warming after ice retreat by only heat conduction (Fig. 9f). The warming front, evident by the turning point to a positive geothermal gradient, is below 50 m in the measured temperature profile and significantly shallower in the results of the conduction model.

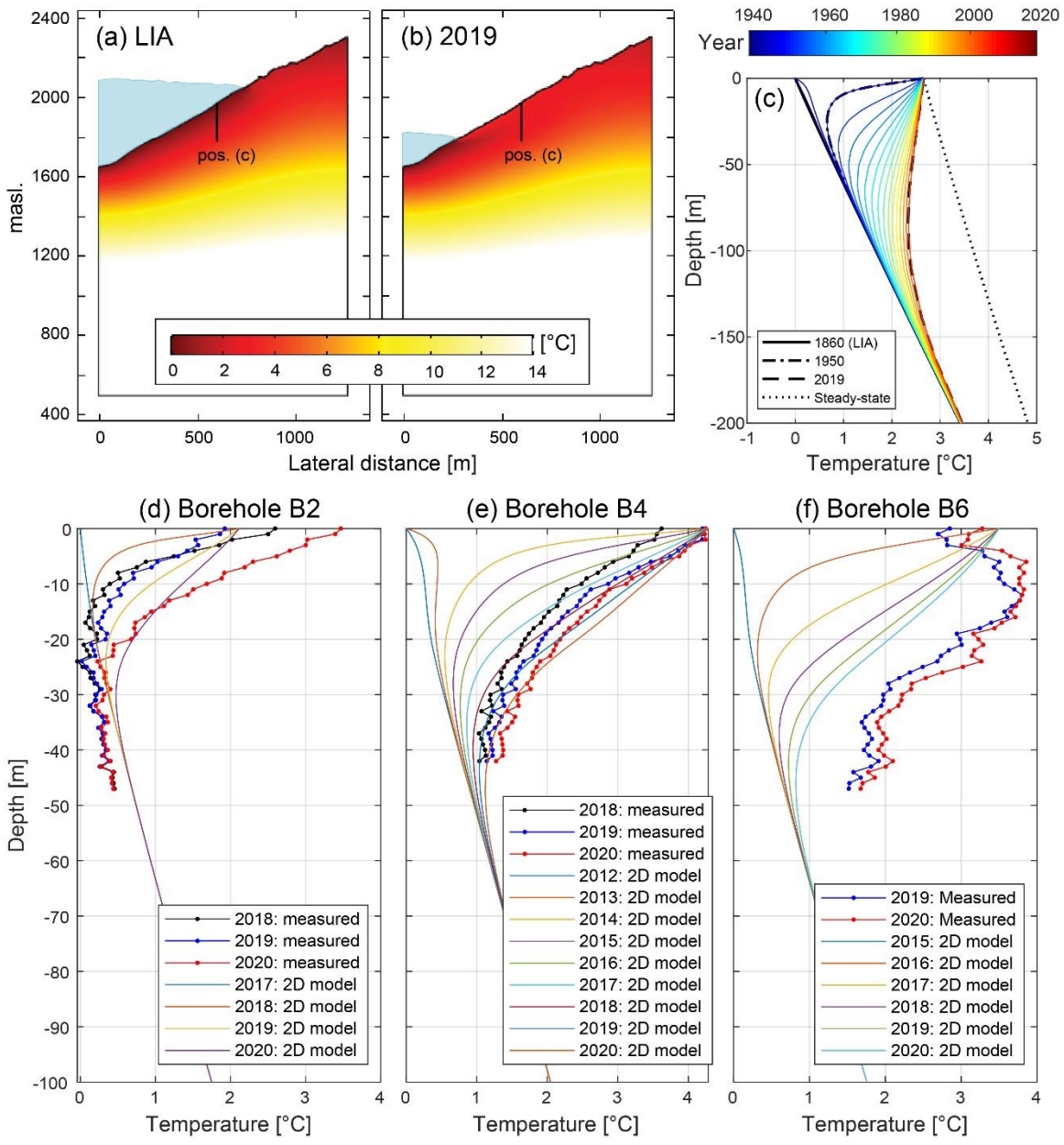

Fig. 9. Results of the transient 2-D numerical model showing the annual mean subsurface temperature field for different ice elevations: (a) LIA ice extent; (b) 2019 ice extent. (c) Evolution of the annual mean subsurface temperature profile from 1860 to 2019 at the indicated mid-slope position c. Graphs d, e, and f show the comparison of the annual mean subsurface temperatures measured at the three borehole locations and the results from the 2-D numerical conduction model.

4.2.2. Drivers of seasonal temperature variations

As described above, the results from the annual mean subsurface temperature simulation show good agreement with the monitoring data in borehole B4 (section 4.2). Therefore, we investigated recent seasonal temperature variations (modelling step 3, section 3.2) at this location, and compared results to monitoring data. Fig. 10 shows a comparison of modelled and measured temperature profiles at different months during the year 2018. The results for other years are similar. The annual surface temperature variability, both in the model and the monitoring data, affects a depth range of approximately 20 m. Measurements and model show a good accordance.

To investigate the mechanisms of seasonal temperature variations in detail, the correlation coefficient between the modeled and measured temperature profile is calculated for each hourly time step and the R-squared value is plotted against time (see Fig. 10g). The small form letters in Fig. 10g indicate the timing of the different panels (Fig. 10a to f). The correlation coefficient time series shows a cyclic behavior with generally very high values (above 0.95) from midsummer to winter. Lower correlation values are observed during spring and temporally correlate with strong pressure head rise in borehole B4, caused by snowmelt infiltration (see Fig. 10g). This negative peak in the R-squared value, however, shows a delay compared to the pressure peak. Daily acquired photos from a time lapse camera installed at the opposite valley flank with view to the borehole locations show that this negative R-squared peak coincides with the time when the rock surface surrounding the borehole becomes snow free.

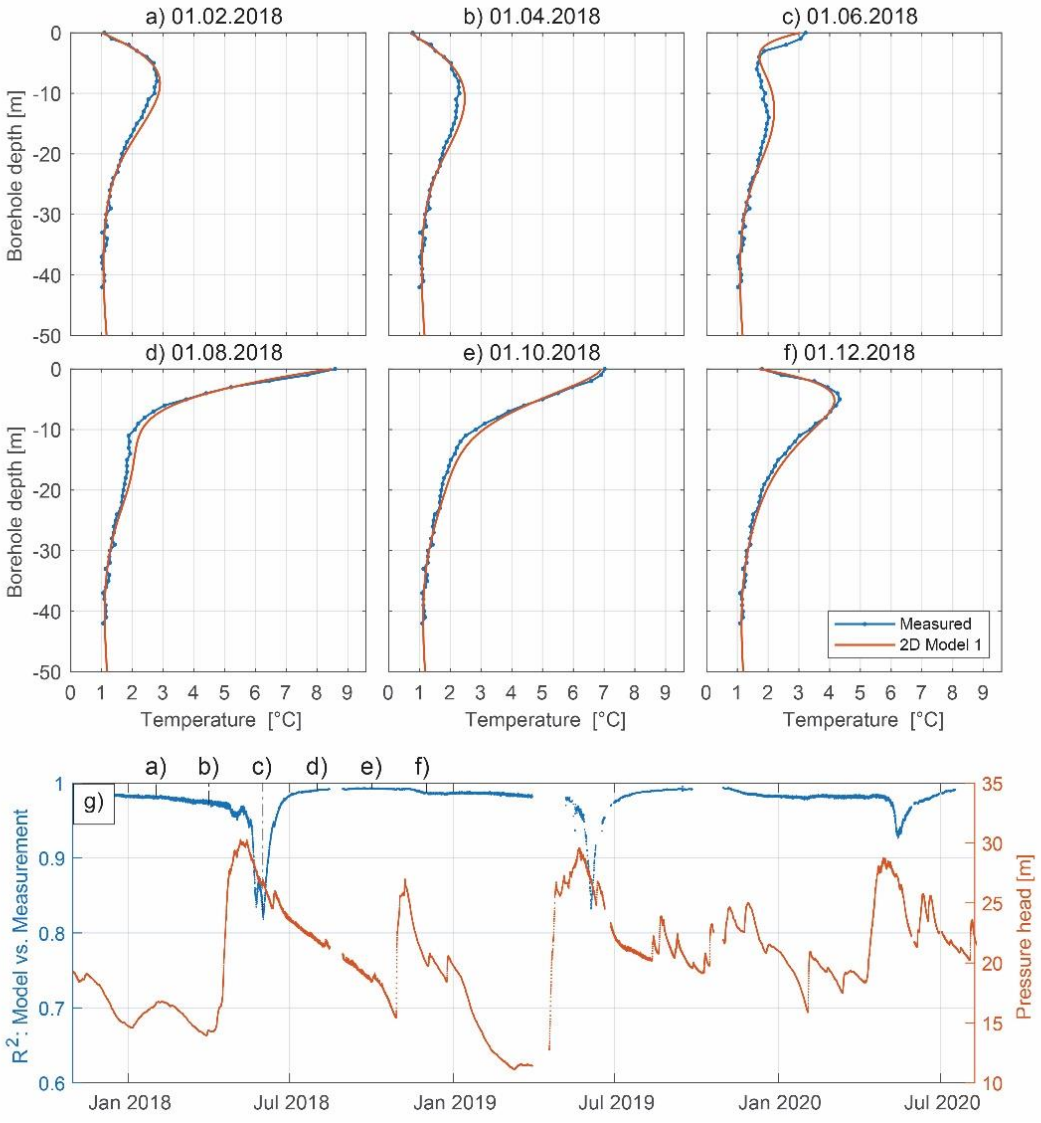

Fig. 10. Panels a to f: Modeled temperature profiles together with the measured subsurface temperature profile at borehole location B4 at specific time steps over the time span of 1 years. Panel g: Correlation (R-squared value) between the measured subsurface temperatures in borehole B4 and the 2D heat conduction model results over time. Additionally, the pressure head measured at the borehole end of B4 is provided. The small form letters indicate the timing of the plots a to f.

4.2.3. Thermoelastic strain

Finally, we investigate the magnitude of thermoelastic strains in the subsurface resulting from seasonal temperature cycles (Fig. 11). This is based on a comparison between monitored and modelled thermoelastic

549 strains in borehole B4 which is dominated by conductive heat transport. In addition, the pressure head
550 measured at the borehole end is provided in the Fig. 11.

551 The results show that the strain signal of the uppermost sensor cannot be reproduced by the simplified
552 thermoelastic continuum model (Fig. 11a). However, strain readings of FBG-sensors number 2 and 3 show
553 a clear annual cyclicity with similar amplitude and phase as the modeled strain (Fig. 11b and c). In the strain
554 signal of sensor 4 (Fig. 11d), a weak cyclic signal with an annual period and an amplitude similar to the
555 modeled one might be present superimposed to another signal strongly correlating with the pressure head.
556 In the deeper FBG-sensors, the modeled thermoelastic strain is an order of magnitude (or more) lower than
557 the actual strain measured in the borehole. Further, the strain variations in these depths often coincide with
558 pressure head fluctuations.

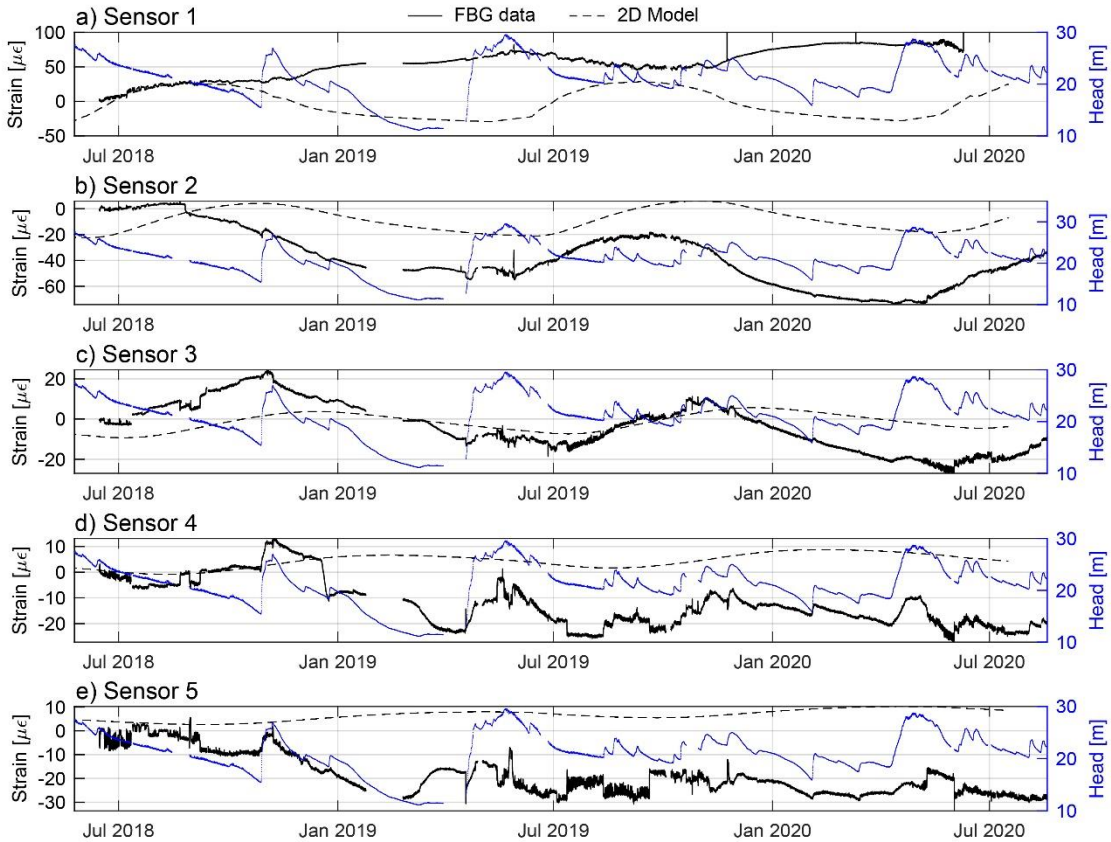

559

Fig. 11. Comparison of the modeled thermo-elastic strain (dashed line), the measured strain in the borehole for the uppermost 5 FBG strain sensors (solid black line), and the pressure head (blue line) measured at the borehole end in borehole B4. Sensor depth intervals: 1: 0 – 4.3 m; 2: 4.3 – 8.6 m; 3: 8.6 – 12.9 m; 4: 12.9 – 17.2 m, 5: 17.2 – 21.5 m.

5. Discussion and interpretation

5.1. Controls on subsurface temperature at a retreating glacier margin

The results in section 4 show that heat transfer by conduction through the rock mass is an important process to explain large parts of the observed subsurface temperature field. Measured temperatures in borehole B4 can be well reproduced with the 2-D heat conduction models and the results for B2 suggest that conduction plays an important role. Conversely, the temperature profile measured in borehole B6 strongly deviates from an expected conduction dominated regime and hence cannot be explained with this process. Additionally, all boreholes display a warming trend, which is likely caused by glacier retreat and subsequent exposure of the slope to annual temperature cycles. The propagation depth of this warming trend is observed to increase in depth the longer a borehole has been ice free.

Non-conductive heat transport processes at our monitoring boreholes are potentially driven by groundwater interaction with the adjacent glacier and yearly recharge cycles on the ice free slope. Typical patterns of such advective temperature disturbances have been discussed by Ge (1998) who distinguishes between (1) distributed vertical groundwater flow in semiconfined porous aquifers, (2) horizontal flow in confined aquifers, and (3) localized groundwater flow in preferential groundwater pathways such as fractures in gneiss and granite, all causing substantially different signatures (Bredehoeft and Papaopulos, 1965; Ge, 1998). Such localized groundwater flow through fractures is assumed to be the cause for the observed positive and negative temperatures anomalies along the profiles (cf. Hugentobler et al., 2020). In order to develop localized thermal anomalies, the water flowing in transmissive fractures has to be in thermal dise-quilibrium with the surrounding rock and must be forced to flow by a natural head gradient, e.g. resulting from a stationary or transient groundwater flow field in an inclined slope.

In borehole B2, Fig. 9d shows a temperature offset of the modeled profile from the measured data of about 0.4° C between depths of 25 m and 50 m. This deviation can be explained by cooling the subsurface with cold water directly connected to glacial ice, which could have caused temperatures of around 0° C down to

a borehole depth of 25 m during the time of ice occupation. We suggest that the high fracture density in this shallow layer (see Fig. 2), as well as the relatively low normal distance (~ 18 m at borehole meter 25) to the rock surface because of the slope steepening below the borehole, enabled efficient advective heat transfer during time of ice occupation and during the years when the glacial ice was still close (i.e., 2018 and 2019). The measured temperature increase at around 25 m that is observed between 2019 and 2020 (*Fig. 4*d) can be related to a decoupling from the advective glacial hydraulic system due to the ongoing ice retreat and an enabling of the penetration of the conductive warming front from the surface.

Relatively minor non-conductive heat transport processes are likely occurring at the B4 borehole location. This is evident when comparing the seasonal variability of the temperature profile measured in the borehole with the 1-D analytical solution and the 2-D numerical modeling results (Figs. 8 and 10). The correlation values reveal an annual repeating decrease during the time of snowmelt in spring, indicating a secondary heat transport process superimposed on the purely conductive transport model (Fig. 10g). Lower correlations are observed in the upper 20 to 30 m of borehole B4. The peak of the reduced correlation values occurs a few weeks after the pore pressure peak (recorded at 43.75 m depth), at a time when the borehole location becomes snow-free. We attribute the observed low correlation to advective heat transfer processes related to water infiltration happening directly at the borehole location.

Borehole B6 temperature measurements cannot be explained using a conduction model, the thermally active layer is 10 m deeper as compared to B2 and B4, and the measurements display larger temperature variations. This borehole is located within an inactive (presumably dormant) landslide body with substantially more disturbed and damaged rock mass compared to the other two borehole locations (cf. section 2). Additionally, a creek fed by nearby regional springs passes through a morphological depression next to the borehole. During drilling in fall 2017, bubbles from the pressurized air used for drilling extruded all around this depression, revealing a high transmissivity in the shallow subsurface. It is assumed that the availability of creek water to infiltrate into the subsurface at this location and higher transmissivity due to the disturbed rock mass enables strong advective heat transfer processes to occur in the shallow subsurface, as documented in Anderson (2005).

5.2. Deformation and implications for rock mass weakening

5.2.1. Strains in the thermally active layer

The analyses of chapter 4.1.3 and 4.2.3 have revealed differences in the drivers of the FBG strain signals as a function of depth, as well as between the borehole locations. All boreholes feature a principal component that displays an annual cyclic strain signal that correlates with ground temperature, and explains between 10 and 20% of the variance in the strain data. Given the correlation to ground temperature, as well as the results of the numerical modeling (Fig. 11, discussed below), it is likely that this component corresponds to thermoelastic deformation. The thermoelastic component is less pronounced in the PCA result of B2, likely because the overall deformation in this borehole is larger than the other two boreholes, and few rapid deformation events dominate the signal (Fig. A 1, Appendix).

The numerical modeling shows that thermoelastic deformation occurs in the thermally active layer, and decreases with depth. This can be clearly observed in our monitoring data of borehole B4 with the most intact rock mass conditions. The FBG data from sensor 2 and 3 (Fig. 11), which correspond to depth intervals of 4.6 to 8.9 m and 8.9 to 13.2 m, show that here the cyclic, thermoelastic deformation signal dominates over other signals. Deeper in the borehole (i.e. from ~ 13.2 m downwards) other signals, that show minor or no correlation with the modeled thermoelastic deformation, dominate the strain time series. In borehole B2 and B6, with less intact rock mass conditions, the uppermost few sensors also show signals with an annual cyclicity that is attributed to thermoelastic effects. However, this continuous cyclic deformation is interrupted by abrupt strain events of similar magnitude or superimposed to sometimes even stronger deformation trends (see Fig. A 1 and A3, Appendix).

An exception is the strain signal measured in the uppermost sensor of all boreholes, which shows an inverse correlation with the model data and hence must be related to a different driving mechanism. Expansion in wintertime and contraction in summertime could be caused by the effect of hygroscopic expansion or moisture induced strain (e.g., Gor et al., 2017) and related to potentially higher relative humidity in the shallow rock layer below the snowpack compared to dry summer conditions. Another possibility to generate extensional strain in wintertime and contraction in summer are frost weathering processes such as volumetric expansion or ice segregation (Draebing et al., 2017). This, however, is unlikely to be the reason for the

640 measured strain at the uppermost sensor as no negative subsurface temperatures were measured in win-
641 tertime.

642 ### 5.2.2. Strains below the thermally active layer

643 Some strain signals measured in deeper sensors clearly correlate with pressure head changes in the bore-
644 hole (e.g. sensor 4 and 5 in Fig. 11) and hence are probably strongly driven by hydromechanical effects.
645 Other sensors show rapid or short-term strain events often temporally coinciding with pressure head
646 changes or precipitation events but overall show a low accordance to the pressure head signal. No individual
647 PCA mode clearly correlates with the measured pressure head, however deformation signals that temporally
648 coincide with pressure head changes are present in several PCA components. We explain this with the
649 more complex nature of hydromechanically coupled deformation in a fractured rock slope and an assumed
650 effect of fluctuating mechanical and hydraulic glacial boundary conditions. Hydromechanically forced strain
651 signals can be substantially different depending on whether the measurement interval is intersecting a trans-
652 missive structure, and on the mode of fracture deformation (Krietsch et al., 2020). Effective glacial ice load
653 changes, due to variations in the subglacial water pressures related to daily meltwater cycles and rainfall
654 infiltration into the glacier during summertime, might be strong enough to cause direct strain and additional
655 hydromechanically coupled effects. Hence, all these processes together are not expected to generate a
656 uniform response that could show a linear correlation with pore pressure. We relate the observed strain
657 events either to poroelastic reactions (showing a strong reversible component and coinciding with pore
658 pressure fluctuations) or to irreversible fracture slip and fracture propagation (damage) driven by pore pres-
659 sure fluctuations or presumably also glacial load changes from varying englacial water pressures. A detailed
660 discussion of hydromechanical drivers for deformation is beyond the scope of the present work but will be
661 explored in a future contribution.

662 The higher number of reversible and irreversible short-term strain events detected in deeper, pore pressure
663 controlled sensors compared to the sensors within the thermally active layer (Fig. 8), can be related to
664 hydromechanical effects. During summer and fall a higher activity in the hydraulic systems of the slope and
665 glacier must be expected, i.e. groundwater recharge by snowmelt and rainfall infiltration induce recharge
666 variations and higher hydraulic gradients in the rock slope, and daily ice melt in summer strongly increases

667 the dynamics of the subglacial hydrological system (Harper et al., 2005). We interpret these effects to be
668 the reason for the observed increased number of strain events occurring during the summer season.

669 ### 5.2.3. Implications for rock mass damage

670 As discussed in the previous section, strain signals during our 2.5-year measurement period are partly
671 driven by thermomechanical and hydromechanical processes. The majority of our detected short-term and
672 rapid strain events coincide with precipitation events, of which about 50 % were strong enough to cause a
673 clear reaction in the pore pressure signal due to infiltration. As discussed above, many of these strain events
674 contain at least a minor irreversible strain contribution, which means that the irreversible deformation is also
675 strongly controlled by hydromechanical effects. This observation agrees with the numerical modeling results
676 of Grämiger et al. (2020), who conclude that hydromechanical effects are more effective in generating long
677 term damage in paraglacial rock slopes compared to thermomechanical effects.

678 The strain time series also contain longer-term irreversible strain trends (predominantly vertical contraction),
679 and 20 to 30 % of the short-term strain events cannot directly be related to any of the investigated drivers.
680 We suggest that these signals may be related to fatigue processes occurring in the studied rock slope. As
681 summarized in the introduction, cyclic stresses can promote fatigue processes and drive damage. In our
682 studied slopes, cyclic loading is mainly driven by annual temperature variations, pore pressure fluctuations
683 and fluctuations of the mechanical load placed on the slope by the Aletsch glacier. In the shallow subsurface,
684 cyclic loading from annual thermoelastic deformation dominates the reversible signal causing largest strain
685 amplitudes of ~ 60 με at an annual cyclicity within the uppermost 4 m and strain amplitudes decreasing with
686 depth (to ~ 5 με at around 20 m depth). Below around 12 m depth, reversible strain cycles that are not
687 related to surface temperature fluctuations and show amplitudes up to ~ 20 με dominate the signal. These
688 cyclic strains are driven by pressure head fluctuations due to snowmelt infiltration or heavy rainfalls and
689 normally occur at frequencies greater than 1/yr. The fact that irreversible strain events are often triggered
690 by similar pressure head magnitudes as the ones causing cyclic reversible deformation, shows that many
691 fractures must be close to a critical stress state. Therefore, we propose that these loading cycles are strong
692 enough to promote progressive damage by cyclic fatigue. This process could also explain the detected
693 short-term strain events that do not temporally coincide with any of the investigated triggers (about 20 - 30

% of all strain events).

The PCA component 1 showing an axial (vertical) overall shortening trend explains the majority of the variance in all three boreholes. Because this signal is mainly irreversible (while the other components often show reversible features) the variance explained by PC1 (50 to 70 %) provides a good estimate for the relative portion of irreversible deformation during our monitoring period. Further, we suggest that the shortening trend in PC1 is composed of (1) a slow, continuous long-term strain signal that can be observed in several sensors (Fig. A 1, A 2, and A 3, Appendix) and (2) the accumulation of major compressive short term strain events (e.g., steps in PC1 of B2, Fig. 7). We relate the irreversible vertical strains in our relatively limited time series to long-term progressive rock mass damage in our deglaciating environment. Compressive strain can originate either from slip along toppling fractures steeply dipping into the slope or from slip along sliding fractures dipping in downslope direction (cf. Fig. 15 in Hugentobler et al., 2020). Fractures of both orientations frequently occur at our study site (Hugentobler et al., 2020). Besides the annual thermo-mechanical and hydromechanical coupled drivers for progressive rock mass damage, longer term stress changes due to unloading from glacial ice downwasting and changes in the thermal and hydraulic boundary conditions connected to the ice retreat might also contribute to this observed deformation (cf. Grämiger et al., 2017; Grämiger et al., 2018; Grämiger et al., 2020).

Finally, we find that the magnitude of measured strain responses depends on the local rock mass quality at the given borehole location. This is observed in our research boreholes, as strong pore pressure variations (e.g. due to the heavy rain storm in early Oct. 2020) cause minor irreversible responses in the more intact rock mass of B4, but very clear irreversible deformation in the more strongly disturbed rock mass around B2. This observation is consistent with the numerical investigations of Gischig et al. (2011a) and Grämiger et al. (2020), who show that the efficiency of thermo-mechanical and hydromechanical loading cycles for fracture propagation (damage) in fractured crystalline rocks strongly depend on the magnitude of the drivers, as well as the initial damage state or criticality of the rock mass.

6. Summary and conclusion

We use three full years of hourly measured borehole temperature and high resolution FBG strain monitoring data to investigate the transient subsurface temperature regime and micrometer-scale deformation in a rock

slope adjacent to a retreating, temperate valley glacier. The presented data give unique new insights into the thermo-mechanical and hydromechanical drivers of rock slope deformation adjacent to retreating glaciers over decadal to seasonal time scales. Detailed analysis and decomposition of the subsurface deformation signals allow to identify various potential drivers for reversible (elastic) and irreversible deformation. This knowledge is important for understanding the main processes contributing to short- and long-term progressive rock mass damage that potentially lead to the formation of paraglacial rock slope instabilities. The most important findings of the present work can be summarized as follows:

1. The thermal investigation reveals that the subsurface temperatures at our monitored slope are currently in a transient state adjusting to new surface temperature conditions after glacial ice retreat. We show that heat conduction is a dominant process and explains most of the observed transient subsurface temperatures at sites with intact rock, however, locally strong deviations from a conduction dominated regime can occur. These deviations can be explained by nonconductive processes (e.g., heat transfer by water) that become important when the rock mass is fractured (i.e., has an increased transmissivity), and are efficient when water and a hydraulic head gradient is available. The observed nonconductive temperature deviations in our study area are related to groundwater exchange with cold subglacial water, snowmelt infiltration, or creek water infiltration.

2. Our strain monitoring data analysis shows that annual surface temperature changes, precipitation events and pore pressure fluctuations are important drivers for deformation at our study site. However, longer-term trends in the strain time series and a minority of short-term strain events cannot directly be related to any of the investigated drivers. We find that thermo-elastic effects due to annual temperature cycles dominate the strain signal in the uppermost 12 m of our stable fractured crystalline rock slope. Below this depth the hydromechanical effects dominate the deformation. Further, we show that both reversible and irreversible short-term deformation more frequently occur during summertime when the hydrological system in the rock slope and in the temperate glacier are more dynamic.

3. Irreversible deformation in our time series, which we relate with progressive rock mass damage, occurs as short-term or rapid strain events within hours or days and as slower, continuous strain

trends (mainly in vertical contraction direction). We show that the majority of short-term strain events coincide with precipitation events or pore pressure changes. Other potential drivers such as extreme surface temperatures or earthquakes occurring in the area do not show temporal correlation with strain events. We propose that cyclic fatigue from above described thermomechanical and hydro-mechanical loading cycles, as well as longer term stress changes related to deglaciation (e.g., glacial ice downwasting and connected changes in thermal, hydraulic and mechanical boundary conditions) can explain both the short-term strain events that do not coincide with any investigated driver, as well as the continuous irreversible strain trends observed in our boreholes.

4. We show that the magnitude of irreversible deformation depends on the magnitude of the driver but also on the spatially variable pre-existing damage at our three borehole locations. At our most stable borehole location, single events with irreversible strain magnitudes are normally on the order of a few με, whereas at the more damaged borehole location irreversible strain magnitudes up to tens or few hundreds of με have been recorded.

Acknowledgements

This project is funded by the Swiss National Science Foundation (project 172492). We want to thank Lukas Frei for his contributions in the framework of his bachelor thesis and Nicolas Oestreicher for sharing time-lapse images from the study site to constrain the timing of snow coverage at the borehole locations. Further, we are grateful for the inputs on the PCA analysis from Nicolas Oestreicher and Clément Roques. Also, we want to thank Reto Seifert and the numerous field helpers who joined our maintenance visits and helped to keep the monitoring system running. Data will be made accessible by acceptance on the ETH Zurich online repository (https://www.research-collection.ethz.ch/).

Appendix A: FBG strain monitoring data

Fig. A 1, A 2, and A 3 contain the temperature corrected hourly mean FBG-strain measurements for each sensor in the three vertical research boreholes. The setup and detailed description of the monitoring system is provided in Hugentobler et al. (2020). All FBG sensors of the three boreholes contain a data gap of about one month in January 2019 which is related to a winter storm that boke the solar panel used for the power supply of the system. A second data gab of around two month duration is existing in FBG monitoring data

of all sensors in borehole B6 in summer 2019 (Fig. A 3). This gap is related to the breakage of the reenforced fiberoptical cable connecting the borehole location to the FBG data acquisition system that happened during a debris flow event. Furthermore, sensor 1 of boreholes B4 and B6 contain incomplete data recordings because of malfunctioning FBG temperature sensors causing traveling reflection peaks that sometimes interfere with the reflected light peaks from the strain sensors because of similar wavelength.

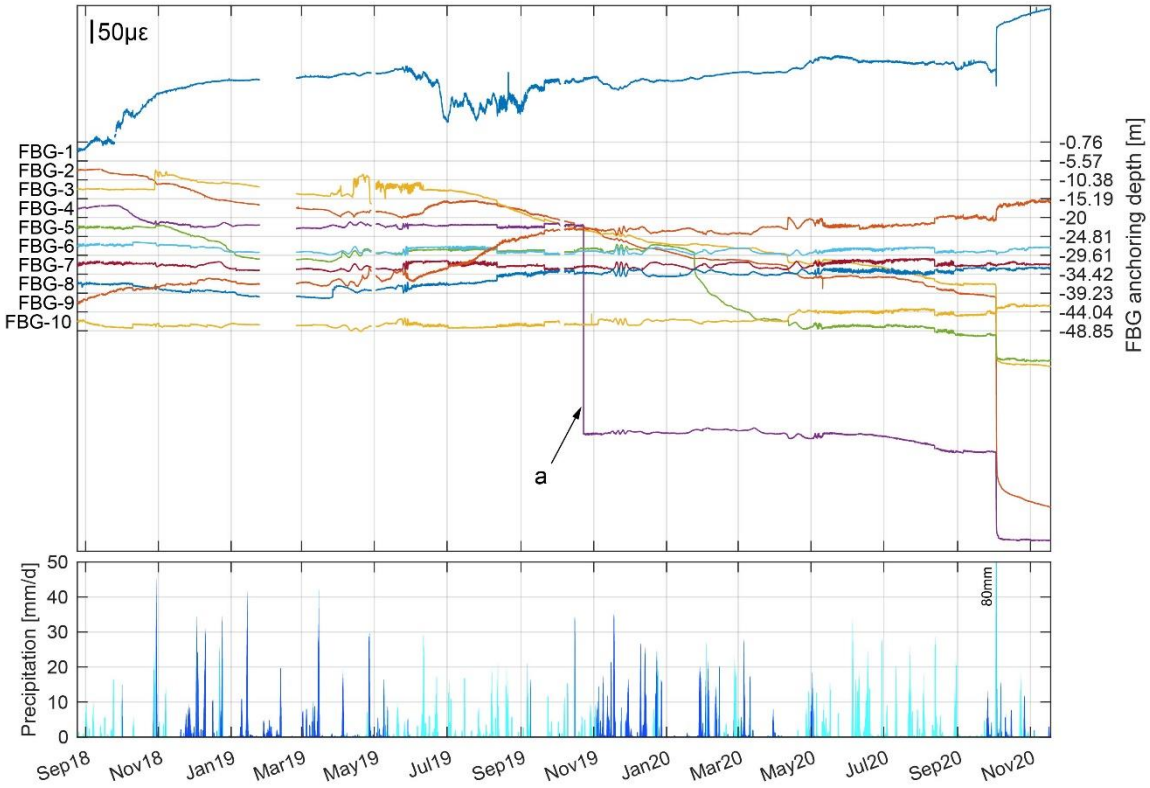

Fig. A 1. Upper plot: The colored lines show a visualization of the temperature corrected strain data of the individual 4.81 m base-length FBG sensors installed in borehole B2. The strain data of each sensor is plotted in the center of the specific depth interval, and the vertical axis ticks correspond to anchoring depth of the FBG sensors. Positive strain means elongation and negative strain compaction of the sensor, and the strain scale is provided on the top left in microstrain (με). (a) Indicated strain step in FBG-4 was identified as a measurement artifact and corrected before the analysis. Lower plot: The vertical bars show the cumulative total precipitation data (per 24 hours) provided by MeteoSchweiz from the weather station "Bruchji" (Valais) located approximately 6 km away from our study site. The blue

colored bars indicate precipitation that presumably occurred as snow (i.e., at surface temperatures below 1°C at our study site (cf. Jennings et al., 2018)).

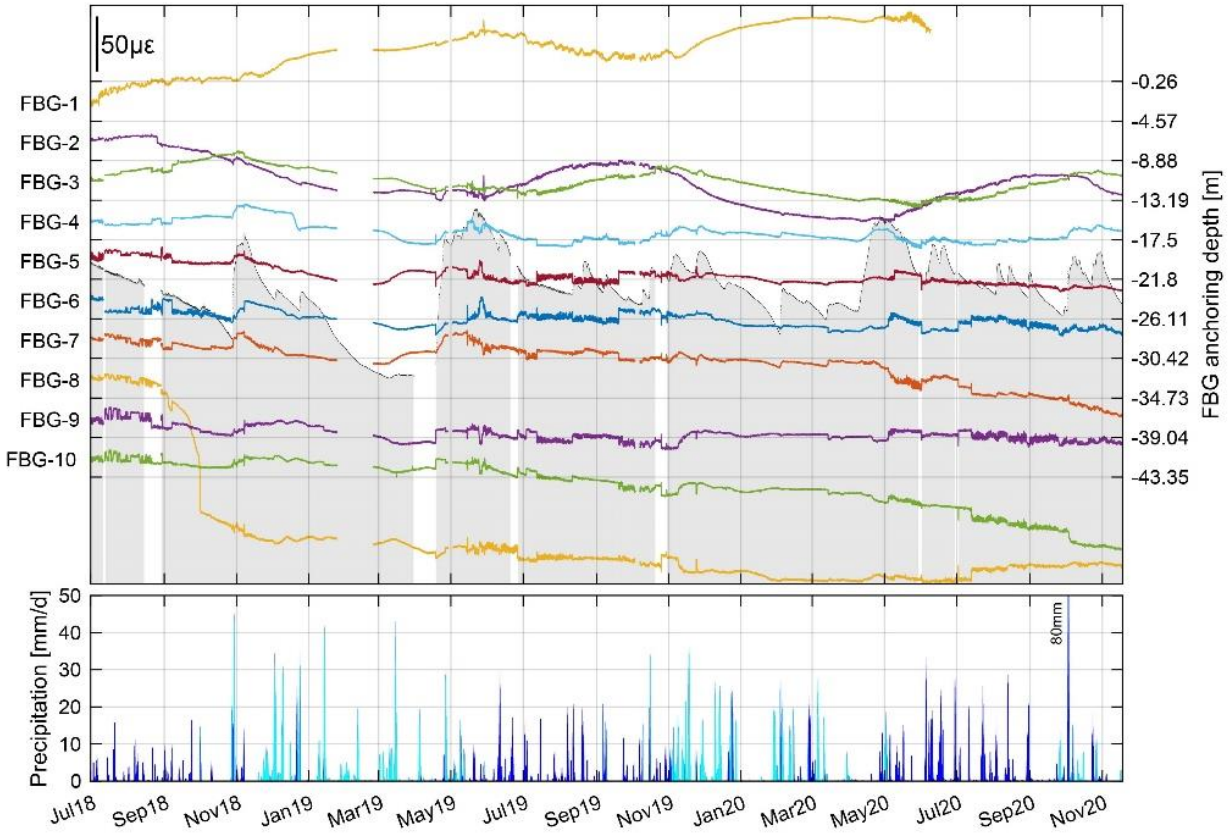

Fig. A 2. Upper plot: The colored lines show a visualization of the temperature corrected strain data of the individual 4.31 m base-length FBG sensors installed in borehole B4. The strain data of each sensor is plotted in the center of the specific depth interval, and the vertical axis ticks correspond to anchoring depth of the FBG sensors. Positive strain means elongation and negative strain compaction of the sensor, and the strain scale is provided on the top left in microstrain (με). Additionally, the elevation of the pressure head in the borehole is provided as a gray area in the background of the plot. Lower plot: The vertical bars show the cumulative total precipitation data (per 24 hours) provided by MeteoSchweiz from the weather station "Bruchji" (Valais) located approximately 6 km away from our study site. The blue colored bars indicate precipitation that presumably occurred as snow (i.e., at surface temperatures below 1°C at our study site (cf. Jennings et al., 2018)).

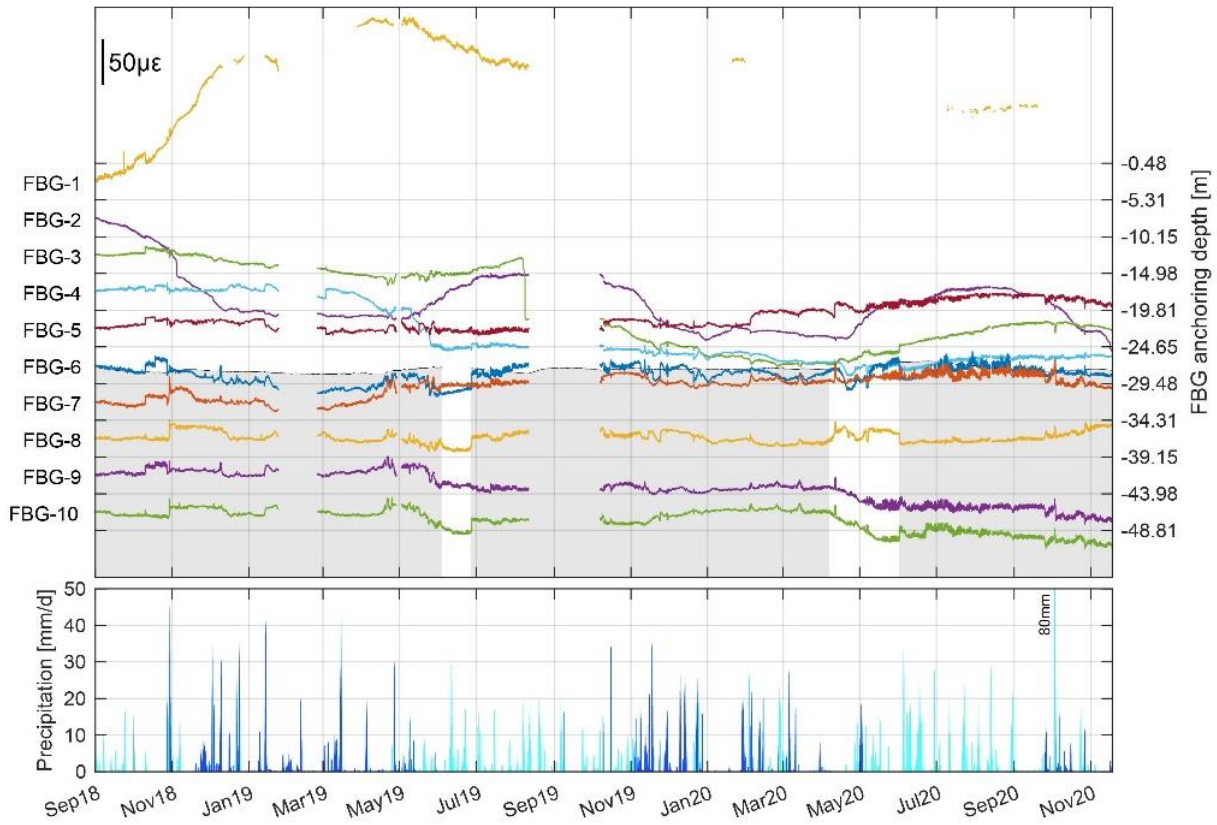

Fig. A 3. Upper plot: The colored lines show a visualization of the temperature corrected strain data of the individual 4.83 m base-length FBG sensors installed in borehole B6. The strain data of each sensor is plotted in the center of the specific depth interval, and the vertical axis ticks correspond to anchoring depth of the FBG sensors. Positive strain means elongation and negative strain compaction of the sensor, and the strain scale is provided on the top left in microstrain (με). Additionally, the elevation of the pressure head in the borehole is provided as a gray area in the background of the plot. Lower plot: The vertical bars show the cumulative total precipitation data (per 24 hours) provided by MeteoSchweiz from the weather station "Bruchji" (Valais) located approximately 6 km away from our study site. The blue colored bars indicate precipitation that presumably occurred as snow (i.e., at surface temperatures below 1°C at our study site (cf. Jennings et al., 2018)).

Appendix B: Earthquake events

In Fig. B 1 all earthquake events used for the comparison with the strain events measured in our research boreholes are characterized by means of earthquake magnitude, epicentral distance to the study site, and

earthquake depth. We used all recorded earthquakes that occurred during our monitoring period with magnitudes greater than M1, epicentral distances of less than 50 km to our study site, and with depth between 0 and 15 km.

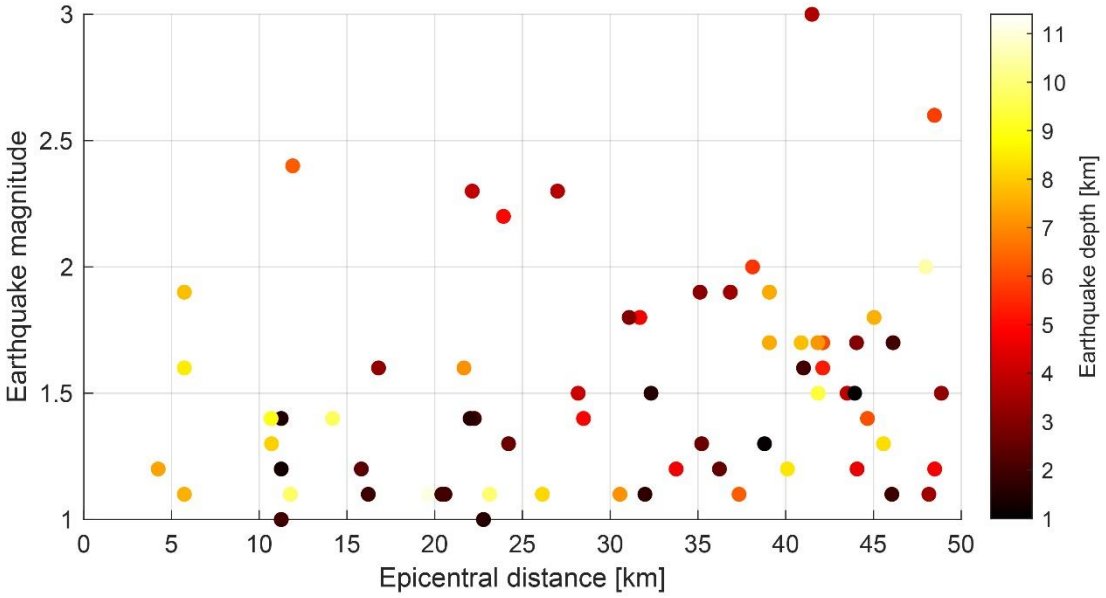

Fig. B 1. Earthquake catalog used for the comparison with strain events detected in our research boreholes (data provided by the Swiss Seismological Service (SED)). The earthquake magnitude is provided vs. the epicentral distance of the individual earthquake event from our study site. Depths information for the individual earthquake events are shown with the color scale.

7. References

Anderson, M. P. (2005), Heat as a ground water tracer, *Ground Water*, *43*(6), 951-968, doi:10.1111/j.1745-6584.2005.00052.x.

Attewell, P. B., and I. W. Farmer (1973), Fatigue behaviour of rock, *International Journal of Rock Mechanics and Mining Sciences & Geomechanics Abstracts*, *10*(1), 1-9, doi:10.1016/0148-9062(73)90055-7.

Baroni, C., S. Martino, M. C. Salvatore, G. S. Mugnozza, and L. Schiliro (2014), Thermomechanical stress-strain numerical modelling of deglaciation since the Last Glacial Maximum in the Adamello Group (Rhaetian Alps, Italy), *Geomorphology*, *226*, 278-299, doi:10.1016/j.geomorph.2014.08.013.

Bodri, L., and V. Čermák (1995), Climate changes of the last millennium inferred from borehole temperatures: Results from the Czech Republic—Part I, *Global Planet Change*, *11*(3), 111-125, doi:10.1016/0921-8181(95)00005-4.

Bodri, L., and V. Čermák (1999), Climate change of the last millennium inferred from borehole temperatures: regional patterns of climatic changes in the Czech Republic — Part III, *Global Planet Change*, *21*(4), 225-235, doi:10.1016/S0921-8181(99)00044-2.
Bredehoeft, J. D., and I. S. Papaopulos (1965), Rates of vertical groundwater movement estimated from the Earth's thermal profile, *Water Resources Research*, *1*(2), 325-328, doi:10.1029/WR001i002p00325.
Brown, E. T., and J. A. Hudson (1973), Fatigue failure characteristics of some models of jointed rock, *Earthquake Engineering & Structural Dynamics*, *2*(4), 379-386, doi:10.1002/eqe.4290020407.
Cerfontaine, B., and F. Collin (2018), Cyclic and Fatigue Behaviour of Rock Materials: Review, Interpretation and Research Perspectives, *Rock Mech Rock Eng*, *51*(2), 391-414, doi:10.1007/s00603-017-1337-5.
Deprez, M., T. De Kock, G. De Schutter, and V. Cnudde (2020), A review on freeze-thaw action and weathering of rocks, *Earth-Sci Rev*, *203*, 103143, doi:10.1016/j.earscirev.2020.103143.
Draebing, D., and M. Krautblatter (2019), The efficacy of frost weathering processes in alpine rockwalls, *Geophys Res Lett*, *46*(12), 6516-6524, doi:10.1029/2019GL081981.
Draebing, D., M. Krautblatter, and T. Hoffmann (2017), Thermo-cryogenic controls of fracture kinematics in permafrost rockwalls, *Geophys Res Lett*, *44*(8), 3535-3544, doi:10.1002/2016gl072050.
Eppes, M. C., and R. Keanini (2017), Mechanical weathering and rock erosion by climate-dependent subcritical cracking, in *Rev. Geophys.*, edited, pp. 470-508, doi:10.1002/2017RG000557.
Ge, S. (1998), Estimation of groundwater velocity in localized fracture zones from well temperature profiles, *Journal of Volcanology and Geothermal Research*, *84*(1), 93-101, doi:10.1016/S0377-0273(98)00032-8.
Gischig, V. S., J. R. Moore, K. F. Evans, F. Amann, and S. Loew (2011a), Thermomechanical forcing of deep rock slope deformation: 1. Conceptual study of a simplified slope, *J Geophys Res-Earth*, *116*, doi:10.1029/2011jf002006.
Gischig, V. S., J. R. Moore, K. F. Evans, F. Amann, and S. Loew (2011b), Thermomechanical forcing of deep rock slope deformation: 2. The Randa rock slope instability, *J Geophys Res-Earth*, *116*, doi:10.1029/2011jf002007.
GLAMOS (1881-2019), The Swiss Glaciers 1880-2016/17, Glaciological Reports No 1-138, Yearbooks of the Cryospheric Commission of the Swiss Academy of Sciences (SCNAT), published since 1964 by VAW / ETH Zurich*Rep.*
GlaThiDa_Consortium (2019), Glacier Thickness Database 3.0.1., edited by W. G. M. Service, Zurich, Switzerland, doi:10.5904/wgms-glathida-2019-03.
Glueer, F., S. Loew, and A. Manconi (2020), Paraglacial history and structure of the Moosfluh Landslide (1850–2016), Switzerland, *Geomorphology*, *355*, 106677, doi:10.1016/j.geomorph.2019.02.021.
Gor, G. Y., P. Huber, and N. Bernstein (2017), Adsorption-induced deformation of nanoporous materials—A review, *Applied Physics Reviews*, *4*(1), 011303, doi:10.1063/1.4975001.
Govaert, G. (2009), *Data analysis*, London : ISTE Wiley.
Grämiger, L. M., J. R. Moore, V. S. Gischig, S. Ivy-Ochs, and S. Loew (2017), Beyond debuttressing: Mechanics of paraglacial rock slope damage during repeat glacial cycles, *J Geophys Res-Earth*, *122*(4), 1004-1036, doi:10.1002/2016jf003967.
Grämiger, L. M., J. R. Moore, V. S. Gischig, and S. Loew (2018), Thermomechanical Stresses Drive Damage of Alpine Valley Rock Walls During Repeat Glacial Cycles, *J Geophys Res-Earth*, *123*(10), 2620-2646, doi:10.1029/2018jf004626.
Grämiger, L. M., J. R. Moore, V. S. Gischig, S. Loew, M. Funk, and P. Limpach (2020), Hydromechanical rock slope damage during Late Pleistocene and Holocene glacial cycles in an

885 Alpine valley, *Journal of Geophysical Research: Earth Surface*, *125*(8),
886 doi:10.1029/2019JF005494.
887 Gruber, S., L. King, T. Kohl, T. Herz, W. Haeberli, and M. Hoelzle (2004), Interpretation of
888 geothermal profiles perturbed by topography: the alpine permafrost boreholes at Stockhorn
889 Plateau, Switzerland, *Permafrost Periglac*, *15*(4), 349-357, doi:10.1002/ppp.503.
890 Guéguen, Y., and V. Palciauskas (1994), *Introduction to the Physics of Rocks*, Princeton
891 University Press.
892 Haberkorn, A., M. Hoelzle, M. Phillips, and R. Kenner (2015), Snow as a driving factor of rock
893 surface temperatures in steep rough rock walls, *Cold Reg Sci Technol*, *118*, 64-75,
894 doi:10.1016/j.coldregions.2015.06.013.
895 Hales, T. C., and J. J. Roering (2007), Climatic controls on frost cracking and implications for the
896 evolution of bedrock landscapes, *J Geophys Res-Earth*, *112*(F2), doi:10.1029/2006jf000616.
897 Harper, J. T., N. F. Humphrey, W. T. Pfeffer, T. Fudge, and S. O'Neel (2005), Evolution of
898 subglacial water pressure along a glacier's length, *Ann Glaciol*, *40*, 31-36,
899 doi:10.3189/172756405781813573.
900 Holzhauser, H., M. Magny, and H. J. Zumbuhl (2005), Glacier and lake-level variations in west-
901 central Europe over the last 3500 years, *Holocene*, *15*(6), 789-801,
902 doi:10.1191/0959683605hl853ra.
903 Hugentobler, M., S. Loew, J. Aaron, C. Roques, and N. Oestreicher (2020), Borehole monitoring
904 of thermo-hydro-mechanical rock slope processes adjacent to an actively retreating glacier,
905 *Geomorphology*, *362*, 107190, doi:10.1016/j.geomorph.2020.107190.
906 Kastrup, U., M. L. Zoback, N. Deichmann, K. F. Evans, D. Giardini, and A. J. Michael (2004),
907 Stress field variations in the Swiss Alps and the northern Alpine foreland derived from inversion of
908 fault plane solutions, *Journal of Geophysical Research: Solid Earth*, *109*(B1),
909 doi:10.1029/2003JB002550.
910 Keusen, H., and J. Amiguet (1987), Die Neubauten auf dem Jungfraujoch. Geologie,
911 Felseigenschaften, Permafrost, *Schweiz. Ing. Archit., 30*, *31*, 17-18.
912 Koo, M.-H., and Y. Song (2008), Estimating apparent thermal diffusivity using temperature time
913 series: A comparison of temperature data measured in KMA boreholes and NGMN wells,
914 *Geosciences Journal*, *12*(3), 255-264, doi:10.1007/s12303-008-0026-5.
915 Krietsch, H., V. S. Gischig, J. Doetsch, K. F. Evans, L. Villiger, M. Jalali, B. Valley, S. Löw, and F.
916 Amann (2020), Hydromechanical processes and their influence on the stimulation effected
917 volume: observations from a decameter-scale hydraulic stimulation project, *Solid Earth*, *11*(5),
918 1699-1729, doi:10.5194/se-11-1699-2020.
919 Lappegard, G., J. Kohler, M. Jackson, and J. O. Hagen (2006), Characteristics of subglacial
920 drainage systems deduced from load-cell measurements, *J Glaciol*, *52*(176), 137-148,
921 doi:10.3189/172756506781828908.
922 McColl, S. T., and D. Draebing (2019), Rock Slope Instability in the Proglacial Zone: State of the
923 Art, in *Geomorphology of Proglacial Systems*, edited by T. Heckmann and D. Morche, pp. 119-
924 140, Springer International Publishing, Cham.
925 Moore, J. R., V. Gischig, M. Katterbach, and S. Loew (2011), Air circulation in deep fractures and
926 the temperature field of an alpine rock slope, *Earth Surf Proc Land*, *36*(15), 1985-1996,
927 doi:10.1002/esp.2217.
928 Pollack, H. N. (1993), Climate-Change Inferred from Borehole Temperatures, *Global Planet*
929 *Change*, *7*(1-3), 173-179, doi:10.1016/0921-8181(93)90048-S.
930 Pollack, H. N., S. Huang, and P.-Y. Shen (1998), Climate change record in subsurface
931 temperatures: a global perspective, *Science*, *282*(5387), 279-281,
932 doi:10.1126/science.282.5387.279
933 Pollack, H. N., and S. P. Huang (2000), Climate reconstruction from subsurface temperatures,
934 *Annu Rev Earth Pl Sc*, *28*, 339-365, doi:10.1146/annurev.earth.28.1.339.

935 Rajeev, P., and J. Kodikara (2016), Estimating apparent thermal diffusivity of soil using field
936 temperature time series, *Geomechanics and Geoengineering*, *11*(1), 28-46,
937 doi:10.1080/17486025.2015.1006266.
938 Rutishauser, A., H. Maurer, and A. Bauder (2016), Helicopter-borne ground-penetrating radar
939 investigations on temperate alpine glaciers: A comparison of different systems and their abilities
940 for bedrock mapping, *Geophysics*, *81*(1), WA119-WA129, doi:10.1190/geo2015-0144.1.
941 Rybach, L., and M. Pfister (1994), Temperature predictions and predictive temperatures in deep
942 tunnels, *Rock Mech Rock Eng*, *27*(2), 77-88, doi:10.1007/BF01020206.
943 Schneider, S., M. Hoelzle, and C. Hauck (2012), Influence of surface and subsurface
944 heterogeneity on observed borehole temperatures at a mountain permafrost site in the Upper
945 Engadine, Swiss Alps, *The Cryosphere*, *6*(2), 517-531, doi:10.5194/tc-6-517-2012.
946 Steck, A. (2011), 1269 Aletschgletscher mit Teil von 1249 Finsteraarhorn, Geolog. Atlas der
947 Schweiz 1:25000.
948 Wegmann, M., and G. H. Gudmundsson (1999), Thermally induced temporal strain variations in
949 rock walls observed at subzero temperatures, *Lect Notes Phys*, *533*, 511-518,
950 doi:10.1007/BFb0104208.
951 Wegmann, M., G. H. Gudmundsson, and W. Haeberli (1998), Permafrost changes in rock walls
952 and the retreat of alpine glaciers: A thermal modelling approach, *Permafrost Periglac*, *9*(1), 23-33,
953 doi:10.1002/(Sici)1099-1530(199801/03)9:1<23::Aid-Ppp274>3.0.Co;2-Y.
954 Wegmann, M. R. (1998), Frostdynamik in hochalpinen Felswänden. am Beispiel der Region
955 Jungfraujoch-Aletsch, ETH Zürich.

956